



# Magneto-fluid-structure interaction issues for vibrating rigid bodies in conducting fluids: The numerical and the analytical approaches

Ming-Jian Li, Nian-Mei Zhang\*, Ming-Jiu Ni\*

School of Engineering Sciences, University of Chinese Academy of Sciences, Beijing 101408, China

## ARTICLE INFO

### Article history:

Received 19 April 2018

Accepted 10 September 2018

Available online 21 September 2018

### Keywords:

Fluid-structure interaction

Benchmark case

Analytical solution

MHD

Magneto-fluid-structure interaction

## ABSTRACT

To study the magneto-fluid-structure interaction (MFSI) problems for rigid bodies and conducting fluids, a numerical method and an analytical approach have been carried out. The numerical scheme is based on a partitioned arbitrary Lagrangian-Eulerian framework, and is suitable for viscous, incompressible magneto-fluid-structure interaction simulation. A displacement prediction-pressure stabilization scheme has been established to enhance the stability and efficiency. Meanwhile, a consistent and conservative scheme for deforming configurations has been developed. This method can numerically ensure the divergence-free condition of the current density, and can conserve the momentum from the Lorentz forces after grids update. The analytical approach has considered a vibrating cylinder surrounded by confined fluids in a magnetic field. By assuming a small amplitude and a low magnetic Reynolds number, the analytical solution can describe the temporal and spatial distribution of the fluid fields, the electromagnetic fields, and the solid motion. These solutions are also suitable for general fluid-structure interaction (FSI) problems. Comparative results suggest good agreement between the two methods developed in this paper. Nonlinear effects of the magnetic fields were presented and discussed based on the numerical results. These cases are based on careful validations, and can hopefully be used for future verification and validation work.

© 2018 Elsevier Ltd. All rights reserved.

## 1. Introduction

Fluid-structure interaction (FSI) phenomena are ubiquitous in industries and our daily lives. From the fluttering of aircraft wings [1], the sloshing of liquid storage tanks [2], to the autumn leaves and our beating hearts [3,4], FSI is almost everywhere. Magneto-hydrodynamics (MHD), a seemingly uncommon problem, has also been developed into a vast field of fundamental and applied research. Typical examples are MHD generators, electromagnetic pumps, and MHD metallurgical applications.

Magneto-fluid-structure interaction (MFSI) refers to the coupling effects of the fluid and solid parts in a magnetic field. This class of problems are rarely covered in the literature, however, are of great importance in the development of fusion reactor blankets. The liquid metal in a blanket bears strong electromagnetic forces, and has mutual influences with the channel and the channel inserts. In such an environment of multi-physical fields, the flow stability, the heat transfer efficiency, and the structural safety issues become rather complicated and challenging. Therefore, a

truly effective and efficient MFSI method, is of great interest and in high demand. Moreover, in other industrial and scientific areas, MFSI studies are expected to increase, e.g., in MHD industries with considerable FSI effects, and in MHD nanofluid studies considering soft channels.

The inherently nonlinear nature of the Navier-Stokes equations places great difficulty to both FSI and MHD analytical studies. Linearization and approximation are often needed. Some examples of FSI analytical work are pipes conveying fluids by Païdoussis et al. [5], slender bodies bending in a cross flow by Luhar et al. [6], fluid-bulkhead vibration with free surface by Hu et al. [7], and flow induced flapping of filaments by Shelley et al. [8]. Classical MHD analytical solutions can be found in the work by Shercliff [9] and Hunt [10], considering MHD channel flows with insulating or conducting walls.

Numerical methods for FSI, on the other hand, have been studied more extensively. Based on the description of fluids, computational FSI can be categorized into three major classes: (1) the Eulerian framework, using non-moving grids and interface capturing techniques, e.g., the immersed boundary method [11], and the volume-of-fluid method [12]; (2) the Lagrangian framework, often using mesh-free methods, e.g., the smoothed particle

\* Corresponding authors.

E-mail addresses: [nmzhang@ucas.ac.cn](mailto:nmzhang@ucas.ac.cn) (N.-M. Zhang), [mjni@ucas.ac.cn](mailto:mjni@ucas.ac.cn) (M.-J. Ni).

hydrodynamics method [13], the moving particle semi-implicit method [14], and the material point method [15]; (3) the mixed method, typically the arbitrary Lagrangian-Eulerian (ALE) method using moving grids [16–19]. Each type of method has its own advantages and limitations. Numerical stability is a great challenge in FSI simulations [20,21], especially for problems with a small solid/fluid density ratio, or a large deformation. In partitioned ALE approaches, iterations often converge very slowly, if at all. Recent attempts to solve this problem include added mass effect treatment and Robin boundary conditions [22,23]. On the other hand, the MHD numerical work, is roughly divided into two classes: the  $B$ -formula scheme [24] and the  $\varphi$ -formula scheme [25]. One of the most challenging parts in a  $\varphi$ -formula method is how to ensure the divergence-free condition of the current flux, and how to conservatively calculate the Lorentz force. Besides, large velocity gradients often occur at the MHD boundary layers, which also causes numerical difficulties.

Analytical and numerical studies for magneto-fluid-structure interaction problems are quite scarce, to the authors' knowledge. It is therefore very necessary to develop new methods, and to build up benchmark cases, for further verification and validation work.

The main objective in this paper, is to establish reliable benchmark cases for incompressible MFSI problems with a small magnetic Reynolds number. The model we are concerned with here is a vibrating cylinder (rigid body) surrounded by confined fluids in a magnetic field. Without magnetic fields, the problem becomes a FSI case, with its solution initially derived by Chen et al. [26] using a linearization to the N-S equations. They compared the theoretical solution to their own experimental results. This work has become very successful as a benchmark test afterwards, and helped to validate a number of FSI solvers. To name a few, we have an ALE streamline upwind/Petrov-Galerkin (SUPG) finite element method by Hughes et al. [27]; monolithic approaches based on the pressure Poisson equation by Ishihara and Yoshimura [28]; a combined edge-based smoothed finite element method and gradient smoothing method (GSM) in an ALE framework by Liu et al. [29], etc. Enlightened by these works, we have derived the analytical solution to the MFSI case, and compared the solution to our numerical method. Moreover, our MFSI solution can directly degenerate into a FSI solution, which differs from Chen et al.'s work, and can be regarded as a correction and extension, with a higher accuracy and a larger range. The numerical method we developed, is based on an ALE framework, with conservative electrical current treatment on deforming grids, and a displacement prediction-pressure stabilization scheme in the iterative process. This numerical solver has been verified by our analytical solution, for both FSI and MFSI cases.

The remainder of the paper is organized as follows. The detailed MFSI numerical method and coupling techniques are given in Section 2. The analytical solution to the magneto-fluid-structure interaction problem is derived in Section 3, which provides the FSI solution at the same time. Then, comparisons between the two methods, as well as the evaluation of the accuracy and efficiency, are presented in Sections 4 and 5. Section 4 focuses on the FSI benchmark cases, explaining the correction and extension work. Section 5 establishes two sets of MFSI benchmark cases, by the analytical and the numerical methods. Section 6 presents more cases considering MFSI effects. Concluding remarks are made in Section 7.

## 2. Numerical methodology

### 2.1. Governing equations

The numerical approach in this paper, is developed for magneto-fluid-structure interaction problems considering coupled

rigid bodies and incompressible electrically conducting fluids. The governing equations are as follows.

At any time  $t \in [0, T]$ , let  $\Omega_f^t$  denote the fluid domain and  $\Omega_s^t$  the solid domain. The fluid-structure interaction interface is defined as  $\Gamma_{\text{FSI}} = \partial\Omega_f^t \cap \partial\Omega_s^t$ , which is the common boundary of the fluid and the solid regions. To describe the deforming fluid domain, define an arbitrary Lagrangian-Eulerian (ALE) mapping  $\mathcal{A}^t$  as

$$\mathcal{A}^t : \Omega_f^0 \rightarrow \Omega_f^t \subset \mathbb{R}^3, \quad \mathbf{x} = \mathcal{A}^t(\mathbf{X}) \in \Omega_f^t, \quad \mathbf{X} \in \Omega_f^0 \quad (1)$$

where  $\Omega_f^0$  and  $\Omega_f^t$  denote the initial and current configurations, respectively.  $\mathbf{x}$  and  $\mathbf{X}$  thus represent coordinates in the corresponding systems. In this ALE description, the Navier-Stokes equations and the continuity equation are then written as:

$$\rho_f \frac{\partial \mathbf{u}_f}{\partial t} \Big|_{\chi} + \rho_f (\mathbf{u}_f - \mathbf{u}_g) \cdot \nabla \mathbf{u}_f = \nabla \cdot \boldsymbol{\sigma}_f + \mathbf{J} \times \mathbf{B} \quad \text{in } \Omega_f^t \times [0, T] \quad (2)$$

$$\nabla \cdot \mathbf{u}_f = 0 \quad \text{in } \Omega_f^t \times [0, T] \quad (3)$$

where  $\rho_f$  is the fluid density and  $\mathbf{u}_f$  is the fluid velocity vector.  $\mathbf{J}$  and  $\mathbf{B}$  represent the current density and the magnetic field, respectively. Subscript  $\chi$  indicates the equations are in the ALE description.  $\mathbf{u}_g$  denotes the velocity of ALE referential system, i.e., the velocity of the deforming fluid grids, satisfying  $\mathbf{u}_g = \partial \mathcal{A}^t(\mathbf{X}) / \partial t$ .  $\boldsymbol{\sigma}_f$  is the fluid stress tensor as  $\boldsymbol{\sigma}_f = -p\mathbf{I} + \eta(\nabla \mathbf{u}_f + \nabla \mathbf{u}_f^T)$ , with  $p$  the fluid pressure,  $\eta$  the dynamic viscosity, and  $\mathbf{I}$  the identity tensor.

For problems with a low magnetic Reynolds number in the scope of this paper, the current density can be calculated by

$$\mathbf{J} = \kappa_f (-\nabla \varphi + \mathbf{u}_f \times \mathbf{B}) \quad \text{in } \Omega_f^t \times [0, T] \quad (4)$$

where  $\varphi$  is the electrical potential and  $\kappa_f$  is the fluid electrical conductivity. The charge conservation is satisfied as

$$\nabla \cdot \mathbf{J} = 0 \quad \text{in } \Omega_f^t \times [0, T] \quad (5)$$

The electric potential Poisson equation is thus obtained from Eqs. (4) and (5):

$$\nabla \cdot (\kappa_f \nabla \varphi) = \nabla \cdot (\kappa_f \mathbf{u}_f \times \mathbf{B}) \quad (6)$$

For the solid domain  $\Omega_s^t$ , neglecting the Lorentz force, the motion equation is given as

$$m_s \frac{\partial^2 \mathbf{d}_s}{\partial t^2} + c_s \frac{\partial \mathbf{d}_s}{\partial t} + k_s \mathbf{d}_s = \mathbf{F}_f \quad \text{in } \Omega_s^t \times [0, T] \quad (7)$$

where  $\mathbf{d}_s$  is the solid displacement vector and  $\mathbf{F}_f$  is the total force vector, which are equivalent to the fluid boundary force. The quantities  $m_s$ ,  $c_s$ , and  $k_s$  represent the mass, damping, and spring stiffness, respectively.

On the fluid-structure interface  $\Gamma_{\text{FSI}}$ , the kinematic boundary condition is satisfied as

$$\mathbf{d}_f = \mathbf{d}_s \quad \text{on } \Gamma_{\text{FSI}} \quad (8)$$

where  $\mathbf{d}_f$  is the fluid displacement vector. The dynamic boundary condition is written as

$$\mathbf{F}_f = \int_{\Gamma_{\text{FSI}}} \boldsymbol{\sigma}_f \mathbf{d}\mathbf{s} \quad (9)$$

where  $\mathbf{s}$  is the area vector of  $\Gamma_{\text{FSI}}$ . The energy conservation on the interface is then satisfied by the virtual work principle.

### 2.2. Displacement prediction-pressure stabilization scheme

Iterative stability is always a great challenge for partitioned FSI approaches. In a MFSI problem, additional variables (the electrical

potential, current density, etc.) cause extra convergence difficulties. During the iteration process, the first few sub-steps within each time level are very likely to be unstable, which may increase the number of sub-steps, or even jeopardize the whole simulation. An inaccurately predicted interface displacement will become an inappropriate initial condition for the next step, and may lead to oscillating pressure results afterwards. Therefore, we developed the following scheme to enhance stability and efficiency of the MFSI algorithm, during the process a displacement prediction–pressure stabilization idea was applied.

This scheme uses a second order prediction in the time domain to get the FSI interface displacement. Taking into account the displacements as well as their time derivatives from previous steps will smoothly provide a predicted displacement, which considers not only the tendency of the interface motion, but also the variation of their tendency. For sub-step  $k$  within time level  $n$ , we first extract solid boundary displacements  $\bar{\mathbf{d}}_s^n$ ,  $\bar{\mathbf{d}}_s^{n-1}$ , and  $\bar{\mathbf{d}}_s^{n-2}$  from the last three time levels  $t_n$ ,  $(t_n - \Delta t)$ , and  $(t_n - 2\Delta t)$ , with overbars indicating converged values. At any time  $t$ , let us assume the fluid displacement to be  $\mathbf{d}_f = \mathfrak{d}(t)$  with a quadratic function  $\mathfrak{d}(\cdot)$ , which can be determined by the displacements from the last three time levels. Then, the fluid displacement  $\mathbf{d}_f^{n+1,k}$  on  $\Gamma_{\text{FSI}}$  for sub-step  $k$  at the next time level can be explicitly predicted by

$$\begin{cases} \mathbf{d}_f^{n+1,k} = \frac{\bar{\mathbf{d}}_s^n - 2\bar{\mathbf{d}}_s^{n-1} + \bar{\mathbf{d}}_s^{n-2}}{(\Delta t)^2} \left( \frac{1}{2} t^2 - t_n t + \frac{1}{2} t \Delta t + \frac{1}{2} t_n^2 - \frac{1}{2} t_n \Delta t \right) \\ \quad + \frac{\bar{\mathbf{d}}_s^n - \bar{\mathbf{d}}_s^{n-1}}{\Delta t} (t - t_n) + \bar{\mathbf{d}}_s^n \quad (k = 0) \\ \mathbf{d}_f^{n+1,k} = \mathbf{d}_f^{n+1,k-1} + \omega^{n,k-1} \mathbf{r}^{n,k-1} \quad (k \neq 0) \end{cases} \quad (10)$$

By taking the time derivative of  $\mathbf{d}_f^{n+1,k}$ , we get the velocity of the fluid boundary surface as:

$$\frac{\partial \mathbf{d}_f^{n+1,0}}{\partial t} = \frac{\bar{\mathbf{d}}_s^n - 2\bar{\mathbf{d}}_s^{n-1} + \bar{\mathbf{d}}_s^{n-2}}{(\Delta t)^2} \left( t - t_n + \frac{1}{2} \Delta t \right) + \frac{\bar{\mathbf{d}}_s^n - \bar{\mathbf{d}}_s^{n-1}}{\Delta t} \quad (11)$$

where  $(\bar{\mathbf{d}}_s^n - 2\bar{\mathbf{d}}_s^{n-1} + \bar{\mathbf{d}}_s^{n-2})/(\Delta t)^2$  and  $(\bar{\mathbf{d}}_s^n - \bar{\mathbf{d}}_s^{n-1})/\Delta t$  can be regarded as the solid acceleration and velocity in a differencing scheme. The solid motion in this way helps to predict the fluid boundary displacement, and to smooth the pressure calculated in the initial steps.

After the initial sub-step prediction, an Aitken's dynamic relaxation [30] is applied to get stable results for the following sub-steps, with a relaxation factor

$$\omega_x^{n,k} = -\omega_x^{n,k-1} \frac{(\mathbf{r}^{n,k-1})^T (\mathbf{r}^{n,k} - \mathbf{r}^{n,k-1})}{(\mathbf{r}^{n,k} - \mathbf{r}^{n,k-1})^T (\mathbf{r}^{n,k} - \mathbf{r}^{n,k-1})} \quad (12)$$

where the residual is  $\mathbf{r}^{n,k} = \mathbf{d}_s^{n+1,k+1} - \mathbf{d}_s^{n+1,k}$ .

Now that we have the fluid boundary displacement  $\mathbf{d}_f^{n+1,k}$ , the grid velocity  $\mathbf{u}_g^{n+1,k}$  on the FSI boundary becomes:

$$\mathbf{u}_g^{n+1,k} = \left( \mathbf{d}_f^{n+1,k} - \bar{\mathbf{d}}_f \right) / \Delta t, \quad \text{on } \Gamma_{\text{FSI}} \quad (13)$$

Applying Eq. (13) as a boundary condition, a Laplacian equation  $\nabla \cdot (\zeta \nabla \mathbf{u}_g^{n+1,k}) = 0$  is solved to obtain the grid velocity in the whole fluid domain. Here, the coefficient  $\zeta = 1/(\|\mathbf{x}_g - \mathbf{x}_{\text{fsi}}\|^2 + \varepsilon_c)$  is a function of distance so that the quality of deformed grids can be controlled, where  $\|\mathbf{x}_g - \mathbf{x}_{\text{fsi}}\|$  denotes the distance between the grid and the FSI boundary, and  $\varepsilon_c$  is a small value. The ALE mapping can thus be written as

$$\mathcal{A}^t(\mathbf{X}) = \mathbf{X} + \mathbf{u}_g^{n+1,k} \Delta t \quad (14)$$

and the spatial position of the fluid domain is therefore determined.

### 2.3. Conservative scheme of current density and Lorentz force for deformed grids

After the ALE mapping, we are now facing the MHD calculation on deformed fluid grids. Based on our previous work [31], we have developed a consistent and conservative scheme on deforming grids system, for MFSI problems.

The divergence-free condition of  $\bar{\mathbf{u}}_f^n$  has been violated after the deformation of the grids. Before dealing with this, let us first solve the electrical potential Poisson equation and calculate the current density. In a controlled volume  $V_c$ , the following discretized equations are solved:

$$\frac{1}{V_c} \sum_{a=1}^{na} \left( \frac{\partial \varphi}{\partial n} \right)_a^{n+1,k} \kappa_f S_a = \frac{1}{V_c} \sum_{a=1}^{na} \mathbf{n}_a \cdot \left( \bar{\mathbf{u}}_f^n \times \mathbf{B} \right)_a \kappa_f S_a \quad (15)$$

$$\mathbf{J}_a^{n+1,k} = -\kappa_f \left( \frac{\partial \varphi}{\partial n} \right)_a^{n+1,k} + \mathbf{n}_a \cdot \left( \bar{\mathbf{u}}_f^n \times \mathbf{B} \right)_a \kappa_f \quad (16)$$

where subscript  $a$  denotes the cell faces and  $na$  is the number of faces.  $S_a$  and  $\mathbf{n}_a$  are the area and the outward direction of a cell face, respectively. A consistent scheme is used for discretizing the electrical potential Eq. (15), and for the calculation of current fluxes (16), such that the divergence-free condition of the current fluxes can be ensured. Meanwhile, for deformed grids, a non-orthogonal correction is needed to get  $\varphi^{n+1,k}$  and  $\mathbf{J}_a^{n+1,k}$ . We then reconstruct the current density to the cell center in the following conservative way:

$$\mathbf{J}_c^{n+1,k} = \frac{1}{V_c} \sum_{a=1}^{na} \mathbf{J}_a^{n+1,k} (\mathbf{x}_a - \mathbf{x}_c) S_a \quad (17)$$

where  $\mathbf{x}_a$  and  $\mathbf{x}_c$  represent the coordinate vectors of cell face center and cell volume center, respectively. Subscript  $c$  denotes the cell volume center. Eq. (17) can ensure the conservation of the total momentum from the Lorentz force.

The pressure implicit split operator (PISO) algorithm [32] is then used to get the fluid velocity and pressure, with the Euler backward scheme:

$$\begin{aligned} & \frac{1}{\Delta t} \left( 1.5 \mathbf{u}_f^* - 2 \bar{\mathbf{u}}_f^n + 0.5 \bar{\mathbf{u}}_f^{n-1} \right)_c V_c + \sum_{a=1}^{na} \mathbf{n}_a \cdot \left( \bar{\mathbf{u}}_f^n - \mathbf{u}_g^{n+1,k} \right)_a S_a \left( \mathbf{u}_f^* \right)_a \\ & = -\frac{1}{\rho_f} (\nabla \bar{p}^n)_c V_c + \frac{1}{\rho_f} \sum_{a=1}^{na} \mathbf{n}_a \cdot \left( \eta \nabla \mathbf{u}_f^* \right)_a^{n+1} S_a + \frac{1}{\rho_f} \left( \mathbf{J}_c^{n+1,k} \times \mathbf{B} \right)_c V_c \end{aligned} \quad (18)$$

$$\nabla \cdot \left( A_c^u \mathbf{u}_f^* \right)_c = \frac{1}{\rho_f} \nabla^2 (p^* - \bar{p}^n)_c \quad (19)$$

where  $\mathbf{u}_f^*$  and  $p^*$  are predicted velocity and pressure, respectively.  $A_c^u$  represents the coefficients after discretization. For several steps of correction, we can get the final velocity  $\mathbf{u}_f^{n+1,k}$  and pressure  $p_f^{n+1,k}$ . The velocity  $\mathbf{u}_f^{n+1,k}$  here satisfies the divergence-free condition, and the Lorentz force conserves the total momentum numerically. Subsequently, the total fluid force exerted on the solid surface can be obtained.

In contrast, a non-conservative scheme, e.g., calculating  $\mathbf{u}_f^{n+1,k}$  after the grid deformation, and before the electrical potential Poisson equation, will violate the divergence-free condition. In this case, Eq. (18) will calculate the Lorentz force with  $\mathbf{J}_c^n$ , which cannot ensure the divergence-free condition on the new configuration. This problem occurs when grids are moving or deforming, and needs to be carefully dealt with. With the conservative scheme mentioned above,  $\varphi^{n+1,k}$  and  $\mathbf{J}_a^{n+1,k}$  are calculated on a new

configuration with corrections, right after the ALE mapping, and can ensure the divergence-free condition of the electrical current.

2.4. Coupling scheme for the conservative magneto-fluid-structure interaction algorithm

After the surface integration of the fluid force, the solid motion equation can be solved. The central differencing scheme is employed and the acceleration and velocity at time level  $n$  are given as

$$\begin{aligned} \frac{\partial^2 \bar{\mathbf{d}}_s^n}{\partial t^2} &= \frac{1}{(\Delta t)^2} (\bar{\mathbf{d}}_s^{n-1} - 2\bar{\mathbf{d}}_s^n + \mathbf{d}_s^{n+1,k+1}), \\ \frac{\partial \bar{\mathbf{d}}_s^n}{\partial t} &= \frac{1}{2\Delta t} (-\bar{\mathbf{d}}_s^{n-1} + \mathbf{d}_s^{n+1,k+1}) \end{aligned} \quad (20)$$

The displacement  $\mathbf{d}_s^{n+1,k+1}$  can then be explicitly obtained by previous results  $\bar{\mathbf{d}}_s^n$  and  $\bar{\mathbf{d}}_s^{n-1}$  as

$$\begin{aligned} \left[ \frac{1}{(\Delta t)^2} m_s + \frac{1}{2\Delta t} c_s \right] \mathbf{d}_s^{n+1,k+1} &= \mathbf{F}_f^n - \left[ k_s - \frac{2}{(\Delta t)^2} m_s \right] \bar{\mathbf{d}}_s^n \\ &\quad - \left[ \frac{1}{(\Delta t)^2} m_s - \frac{1}{2\Delta t} c_s \right] \bar{\mathbf{d}}_s^{n-1} \end{aligned} \quad (21)$$

Now that all necessary solvers have been introduced, we summarize the entire algorithm in Table 1, which provides the procedures of the iterative approach within time level  $n$ .

In Table 1, all unknown variables are at the left hand side, while right-hand-side variables are known from previous steps. These variables have been defined above. The hollow capital letters  $\mathbb{D}, \mathbb{M}, \mathbb{E}, \mathbb{J}, \mathbb{N}, \mathbb{P}, \mathbb{F}, \mathbb{S}$  are for functions and solvers, which have been introduced in Eqs. (10), (13), (15)–(19), (9), (21). The maximum convergence tolerance is indicated by  $\varepsilon_{\max}$ .

3. Analytical study on the strong coupled MFSI problem

3.1. Description of the problem

Consider a rigid cylinder vibrating with a small amplitude in a cylindrical container, and a viscous, incompressible, and electrically conducting fluid filling the container and surrounding the cylinder (Fig. 1). Let us establish a Cartesian coordinate system  $(x, y, z)$  with a basis vector  $(\hat{\mathbf{e}}_x, \hat{\mathbf{e}}_y, \hat{\mathbf{e}}_z)$  to describe the solid part, and a cylindrical coordinate system  $(r, \theta, z)$  with a basis vector

$(\hat{\mathbf{e}}_r, \hat{\mathbf{e}}_\theta, \hat{\mathbf{e}}_z)$  to describe the fluid. Both coordinate systems have their origins fixed at the center of the cylinder. The container and the cylinder are infinitely long in the  $z$ -direction, and their radiuses are respectively  $R_1$  and  $R_2$ . The cylinder is attached to the fixed, no-slip container wall by a virtual spring (one can regard the spring as an approximation to elastic forces of a rod with clamped ends). In the  $z$ -direction, an external magnetic field is applied, with a constant magnitude of  $B_0$ . At the initial time  $t = 0$ , a small displacement  $\Delta l$  is given to the cylinder, which sits in the initially quiescent fluid.

3.2. Formulation and derivation

For any time  $t \in [0, T]$ , taking into account the fluid influence, the motion equation of the cylinder is given by:

$$m_s \frac{\partial^2 \mathbf{d}_s}{\partial t^2} + c_s \frac{\partial \mathbf{d}_s}{\partial t} + k_s \mathbf{d}_s = \mathbf{F}_f \quad (22)$$

where  $m_s$  is the mass,  $c_s$  is the inherent damping, and  $k_s$  is the spring stiffness.  $\mathbf{d}_s$  denotes the displacement vector, which is only in the  $x$ -direction here.  $\mathbf{F}_f$  represents the total external fluid force, including the pressure and the viscous force. Due to the symmetry,  $\mathbf{F}_f$  is also in the  $x$ -direction only, and can be further separated into two parts: (1) the part in phase with the solid acceleration, representing the added mass effect; (2) the part in phase with the solid velocity, indicating the added damping effect. Defining  $C_M$  and  $C_V$  as the added mass and added damping coefficients, respectively, we can then re-write Eq. (22) into the following free vibration formula:

$$(m_s + C_M M) \frac{\partial^2 \mathbf{d}_s}{\partial t^2} + (c_s + C_V M \omega) \frac{\partial \mathbf{d}_s}{\partial t} + k_s \mathbf{d}_s = 0 \quad (23)$$

with  $M = \rho_f \pi R_1^2$  the virtual fluid mass displaced by the cylinder, and  $\rho_f$  the fluid density. The quantity  $\omega$  denotes the damped vibrating frequency of the cylinder as

Table 1  
Iterative algorithm for magneto-fluid-structure interaction problems.

Sub-iterations at the $n$ th time level	
1:	Predict fluid boundary displacement $\mathbf{d}_f^{n+1,k} = \mathbb{D}(\bar{\mathbf{d}}_s^n, \bar{\mathbf{d}}_s^{n-1}, \bar{\mathbf{d}}_s^{n-2}, \mathbf{r}^{n,k-1})$
2:	Update the configuration with grids velocity $\mathbf{u}_g^{n+1,k} = \mathbb{M}(\mathbf{d}_f^{n+1,k}, \bar{\mathbf{d}}_s^n)$
3:	Solve electrical potential Poisson equation, get $\varphi^{n+1,k} = \mathbb{E}(\bar{\mathbf{u}}_f^n)$
4:	Calculate and reconstruct the electrical current $\mathbf{J}^{n+1,k} = \mathbb{J}(\varphi^{n+1,k})$
5:	Solve N-S equations and the pressure Poisson equation, get velocity $\mathbf{u}_f^{n+1,k} = \mathbb{N}(\bar{\mathbf{u}}_f^n, \bar{\mathbf{u}}_f^{n-1}, \mathbf{u}_g^{n+1,k}, \mathbf{J}^{n+1,k})$ and pressure $p_f^{n+1,k} = \mathbb{P}(\mathbf{u}_f^{n+1,k})$
6:	Integrate FSI boundary total force $\mathbf{F}_f^{n+1,k} = \mathbb{F}(p_f^{n+1,k}, \mathbf{u}_f^{n+1,k})$
7:	Solve the solid motion equation, get $\mathbf{d}_s^{n+1,k+1} = \mathbb{S}(\mathbf{F}_f^{n+1,k}, \bar{\mathbf{d}}_s^n, \bar{\mathbf{d}}_s^{n-1})$
8:	Get residual $\mathbf{r}^{n,k} = \mathbf{d}_s^{n+1,k+1} - \mathbf{d}_s^{n+1,k}$
9:	Convergence criterion. If $\ \mathbf{r}^{n,k}\ _2 > \varepsilon_{\max}$ , not converged, go to step 10. If $\ \mathbf{r}^{n,k}\ _2 \leq \varepsilon_{\max}$ , converged, go to step 11.
10:	$k = k + 1$ , go to next sub-step and repeat 1–9.
11:	Update $\bar{\mathbf{d}}_s^{n+1} = \mathbf{d}_s^{n+1,k+1}$ , and $\bar{\mathbf{u}}_f^{n+1} = \mathbf{u}_f^{n+1,k}$
12:	$n = n + 1$ , go to next time level and repeat 1–9.

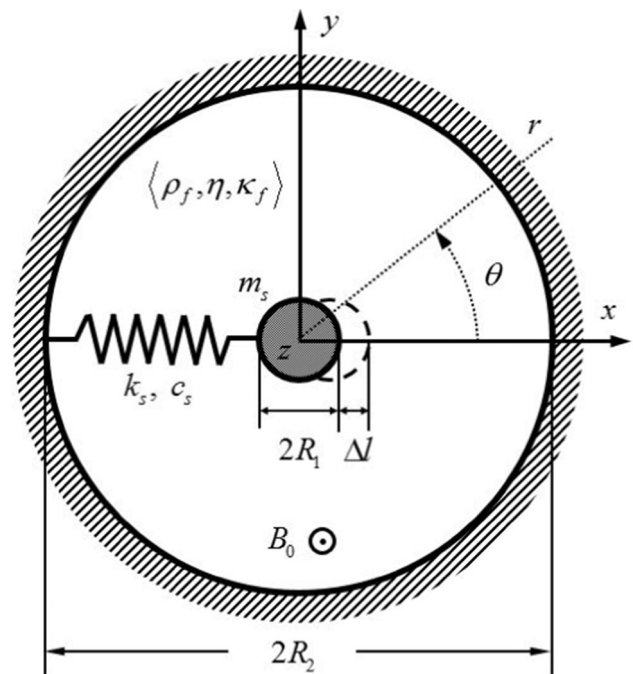


Fig. 1. The vibrating cylinder surrounded by an electrically conducting fluid in a magnetic field.

$$\omega = \sqrt{\frac{k_s(1 - \zeta^2)}{m_s + C_M M}} \quad (24)$$

where  $\zeta$  is the damping ratio and satisfies

$$\zeta = \frac{c_s + C_V M \omega}{2\sqrt{k_s(m_s + C_M M)}} \quad (25)$$

By introducing a parameter  $\lambda$ , the general solution to Eq. (23) takes the form  $\mathbf{d}_s = (D_1 e^{-\lambda t + i\omega t} + D_2 e^{-\lambda t - i\omega t}) \hat{\mathbf{e}}_x$  with complex constants  $D_i$ .  $\lambda$  governs the amplitude increment or decrement, and meets

$$\lambda = \frac{\zeta}{\sqrt{1 - \zeta^2}} \omega \quad (26)$$

By determining the constants  $D_i$  with initial conditions

$$\mathbf{d}_s|_{t=0} = \Delta l \hat{\mathbf{e}}_x, \quad \text{and} \quad \frac{\partial \mathbf{d}_s}{\partial t} \Big|_{t=0} = 0 \quad (27)$$

we then write the displacement of the cylinder as:

$$\mathbf{d}_s = \Delta l \cdot e^{-\lambda t} \left( \cos \omega t + \frac{\lambda}{\omega} \sin \omega t \right) \hat{\mathbf{e}}_x \quad (28)$$

The solid velocity is thus  $\mathbf{u}_s = \partial \mathbf{d}_s / \partial t = -[(\lambda^2 + \omega^2) / \omega] \Delta l e^{-\lambda t} \sin \omega t \hat{\mathbf{e}}_x$ . Without loss of generality, let us write the solid velocity in the complex domain as

$$\mathbf{u}_s = -\frac{(\lambda^2 + \omega^2) \Delta l}{\omega} e^{-\lambda t + i\omega t} \hat{\mathbf{e}}_x \quad (29)$$

whose imaginary part is equivalent to the time derivative of Eq. (28). The time varying features of the fluid domain can subsequently be described by  $e^{-\lambda t + i\omega t}$ .

On the fluid-structure interaction boundary, i.e., the cylinder surface, the kinematic boundary satisfies

$$\mathbf{u}_f|_{r=R_1} = \mathbf{u}_s \quad (30)$$

where  $\mathbf{u}_f$  is the fluid velocity vector. A coordinate transformation is needed in Eq. (30), since different coordinate systems are used. On the container wall, the no-slip boundary condition is:

$$\mathbf{u}_f|_{r=R_2} = 0 \quad (31)$$

For the fluid domain, the continuity equation has already been provided in Eq. (3), and the Navier-Stokes equation is re-written as:

$$\rho_f \frac{\partial \mathbf{u}_f}{\partial t} = -\nabla p + \eta \nabla^2 \mathbf{u}_f + \mathbf{J} \times \mathbf{B} \quad (32)$$

where the constant external magnetic field is  $\mathbf{B} = B_0 \hat{\mathbf{e}}_z$ ,  $\mathbf{J}$  denotes the current density, and  $\mathbf{J} \times \mathbf{B}$  represents the Lorentz force.

To solve Eq. (32), let us introduce a function  $\psi(r, \theta, t)$  which meets

$$\mathbf{u}_f = -\frac{\partial \psi}{r \partial \theta} \hat{\mathbf{e}}_r + \frac{\partial \psi}{\partial r} \hat{\mathbf{e}}_\theta \quad (33)$$

Function  $\psi$  therefore satisfies the continuity Eq. (3). Substituting Eq. (33) into Eq. (32), and taking the curl of Eq. (32), we can eliminate the pressure as well as the Lorentz force. The following equation is subsequently obtained:

$$\nabla^4 \psi - \frac{\rho_f}{\eta} \frac{\partial}{\partial t} \nabla^2 \psi = 0 \quad (34)$$

The solution to Eq. (34) takes the form

$$\psi = -\frac{(\lambda^2 + \omega^2) \Delta l}{\omega} \left\{ \left( \frac{C_1 R_1^2}{r} + C_2 r \right) + R_1 [C_3 I_1(\xi r) + C_4 K_1(\xi r)] \right\} \sin \theta e^{-\lambda t + i\omega t} \quad (35)$$

where  $I_i$  and  $K_i$  are modified Bessel functions.  $C_i$  are undetermined parameters, and  $\xi = \sqrt{(-\lambda + i\omega) \rho_f / \eta}$ .

From Eqs. (33) and (35), the fluid velocity can be obtained:

$$\begin{aligned} \mathbf{u}_f = & -\frac{(\lambda^2 + \omega^2) \Delta l}{\omega} \left[ -C_1 \left( \frac{R_1}{r} \right)^2 - C_2 - \frac{R_1}{r} C_3 I_1(\xi r) \right. \\ & \left. - \frac{R_1}{r} C_4 K_1(\xi r) \right] \cos \theta e^{-\lambda t + i\omega t} \hat{\mathbf{e}}_r - \frac{(\lambda^2 + \omega^2) \Delta l}{\omega} \left\{ -C_1 \left( \frac{R_1}{r} \right)^2 \right. \\ & \left. + C_2 + C_3 \left[ \alpha I_0(\xi r) - \frac{R_1}{r} I_1(\xi r) \right] \right. \\ & \left. + C_4 \left[ -\alpha K_0(\xi r) - \frac{R_1}{r} K_1(\xi r) \right] \right\} \sin \theta e^{-\lambda t + i\omega t} \hat{\mathbf{e}}_\theta \quad (36) \end{aligned}$$

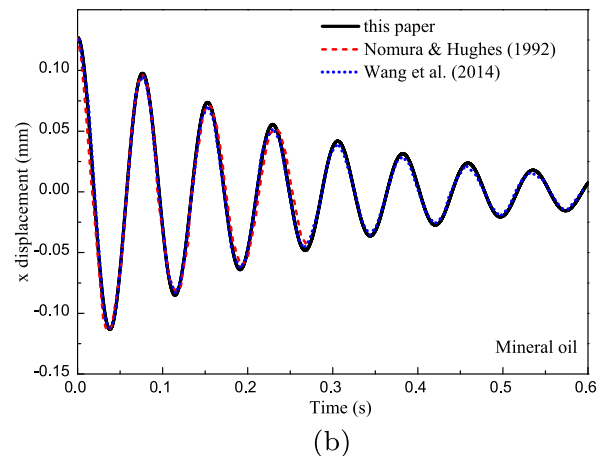
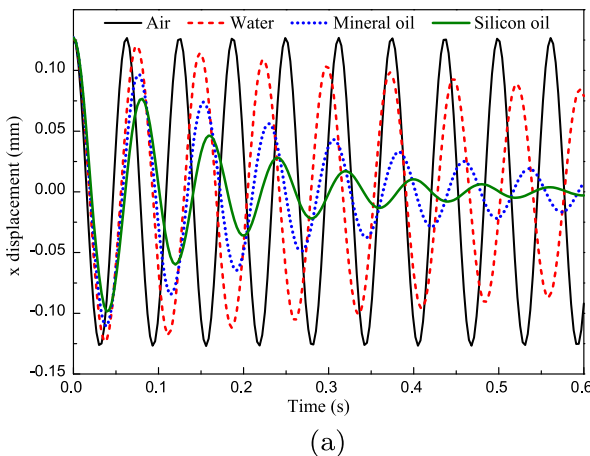
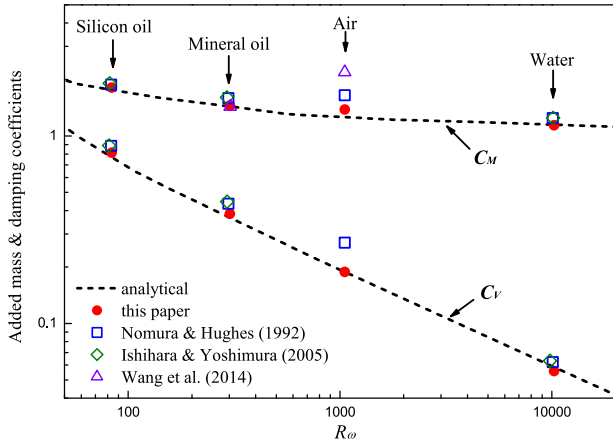


Fig. 2. Displacement histories for FSI cases: (a) analytical results for all four types of fluids; (b) numerical results for mineral oil compared with the literature.



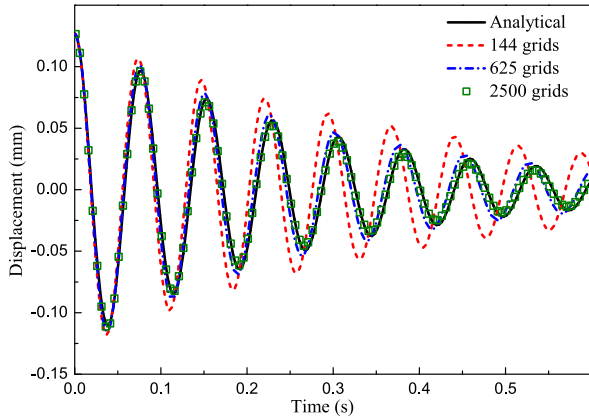
**Fig. 3.** Added mass and damping coefficients by our numerical method, compared with the analytical solution and the numerical results in [27–29].

In Eq. (36), no explicit Lorentz force terms exist. The electromagnetic effect actually lies in the parameters  $\lambda$  and  $\omega$ , which suggest an implicit relation between the fluid velocity and the Lorentz force. By applying the boundary conditions Eqs. (30) and (31), the parameters  $C_i$  in Eq. (36) are determined:

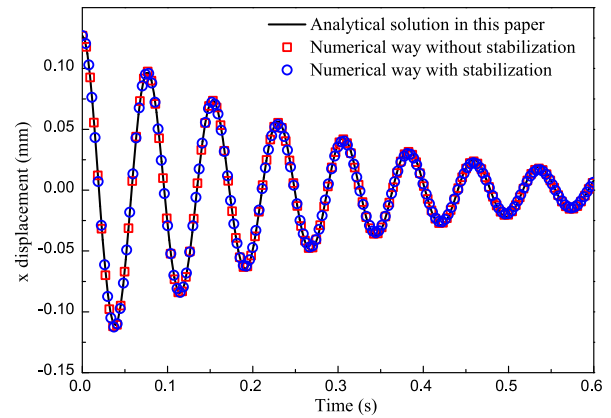
$$\begin{aligned}
 C_1 &= \{-\alpha^2[I_0(\alpha)K_0(\beta) - I_0(\beta)K_0(\alpha)] + 2\alpha[I_1(\alpha)K_0(\beta) + I_0(\beta)K_1(\alpha)] \\
 &\quad - 2\alpha\gamma[I_0(\alpha)K_1(\beta) + I_1(\beta)K_0(\alpha)] + 4\gamma[I_1(\alpha)K_1(\beta) - I_1(\beta)K_1(\alpha)]\}/C_5 \\
 C_2 &= \{2\alpha\gamma[I_1(\beta)K_0(\beta) - I_0(\beta)K_1(\beta)] + \alpha^2\gamma^2[I_0(\alpha)K_0(\beta) - I_0(\beta)K_0(\alpha)] \\
 &\quad - 2\alpha\gamma^2[I_1(\alpha)K_0(\beta) + I_0(\beta)K_1(\alpha)]\}/C_5 \\
 C_3 &= \{-2\alpha K_0(\beta) - 4\gamma K_1(\beta) + \gamma^2[2\alpha K_0(\alpha) + 4K_1(\alpha)]\}/C_5 \\
 C_4 &= \{-2\alpha I_0(\beta) + 4\gamma I_1(\beta) + \gamma^2[2\alpha I_0(\alpha) - 4I_1(\alpha)]\}/C_5 \\
 C_5 &= \alpha^2(1 - \gamma^2)[I_0(\alpha)K_0(\beta) - I_0(\beta)K_0(\alpha)] \\
 &\quad + 2\alpha\gamma[I_0(\alpha)K_1(\beta) - I_1(\beta)K_0(\beta) + I_1(\beta)K_0(\alpha) - I_0(\beta)K_1(\beta)] \\
 &\quad + 2\alpha\gamma^2[I_0(\beta)K_1(\alpha) - I_0(\alpha)K_1(\alpha) + I_1(\alpha)K_0(\beta) - I_1(\alpha)K_0(\alpha)]
 \end{aligned} \tag{37}$$

where  $\alpha = \xi R_1$ ,  $\beta = \xi R_2$ , and  $\gamma = R_1/R_2$ . In a traditional approach, these parameters are constant. Contrarily,  $C_i$  here are relevant to the vibration features, and are determined by the factors like the fluid density, the viscosity and the initial state of the cylinder.

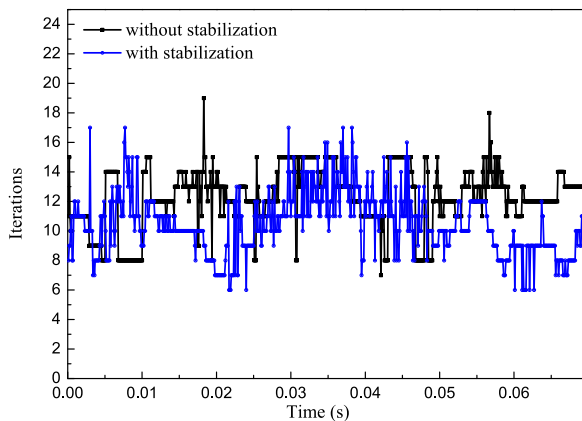
The Ohm's law and the charge conservation law have been provided in Eqs. (4) and (5). Combining these equations with Eq. (33), the electrical potential Poisson equation will be obtained in a very concise form:



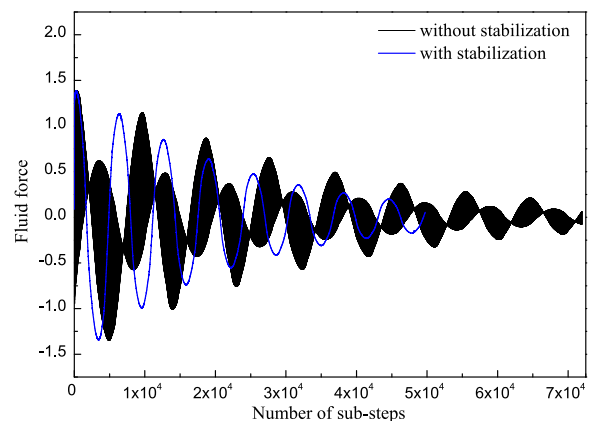
(a)



(b)



(c)



(d)

**Fig. 4.** Accuracy and efficiency of the numerical method. (a) The spatial convergence. (b) Displacement histories with/without the stabilization scheme. (c) The number of sub-steps within each time level. (d) The fluid total force during the iterative calculation.

**Table 2**  
Added mass and damping coefficients for FSI benchmark cases.

		Air	Water	Mineral oil	Silicon oil
$C_M$	$R_\omega$	1054	10236	302	84
	Re	10.54	102.36	3.02	0.84
	$\omega$	100.75	84.40	82.13	78.57
	Chen et al.	1.2739	1.1393	1.4045	1.6796
	Analytical in this present	1.2739	1.1447	1.4468	1.7857
$C_V$	Numerical in this present	1.3845	1.1406	1.4529	1.8125
	Chen et al.	0.1926	0.0561	0.3271	0.6182
	Analytical in this present	0.1926	0.0616	0.3711	0.7330
	Numerical in this present	0.1883	0.0558	0.3848	0.8141

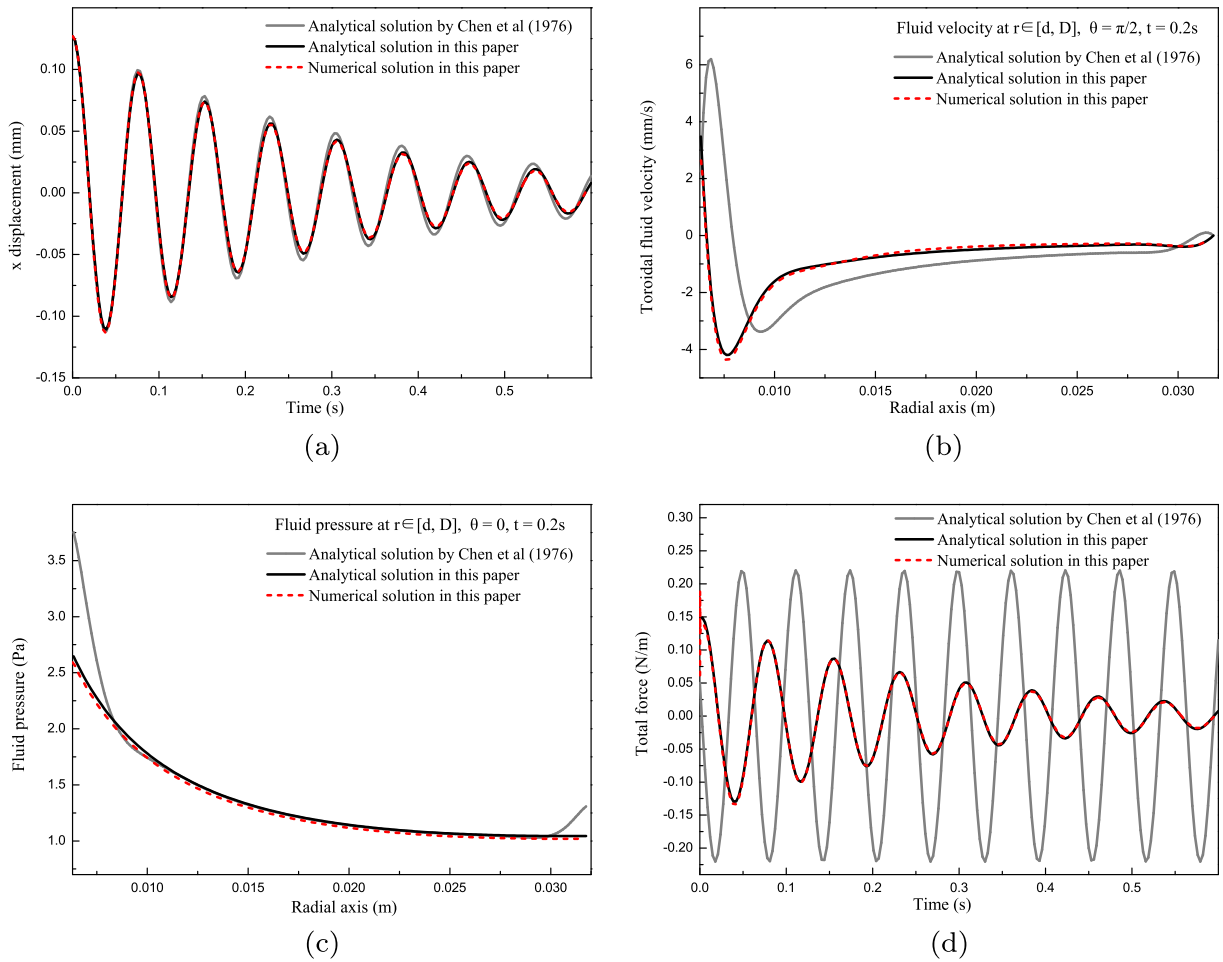


**Fig. 5.** Comparison between our analytical solution and numerical solution, with Chen et al.'s analytical solution. (a) The solid displacement history. (b) The fluid velocity. (c) The fluid pressure. (d) The total fluid force exerted on the solid surface. The time and spatial position are noted in the figures.

$$\nabla^2 \varphi = B_0 \nabla^2 \psi \tag{38}$$

The solution to Eq. (38) takes the form

$$\varphi = -\frac{(\lambda^2 + \omega^2) \Delta l}{\omega} B_0 \left[ E_1 \frac{R_1^2}{r} + E_2 r + C_1 \frac{R_1^2}{r} + C_2 r + R_1 C_3 I_1(\zeta r) + R_1 C_4 K_1(\zeta r) \right] \sin \theta e^{-\lambda t + i \omega t} \tag{39}$$

where  $C_i$  are known in Eqs. (37), and  $E_i$  are additional constants. Let us apply the following electric potential boundary conditions

$$\frac{\partial \varphi}{\partial r} \Big|_{r=R_1} = 0, \quad \text{and} \quad \varphi \Big|_{r=R_2} = 0 \tag{40}$$

and the constants  $E_i$  can therefore be determined as

$$E_1 = -\frac{R_2^2}{R_2^2 + R_1^2}, \quad E_2 = \frac{R_1^2}{R_2^2 + R_1^2} \tag{41}$$

Substituting Eqs. (36) and (39) into (4), the current density can be obtained as

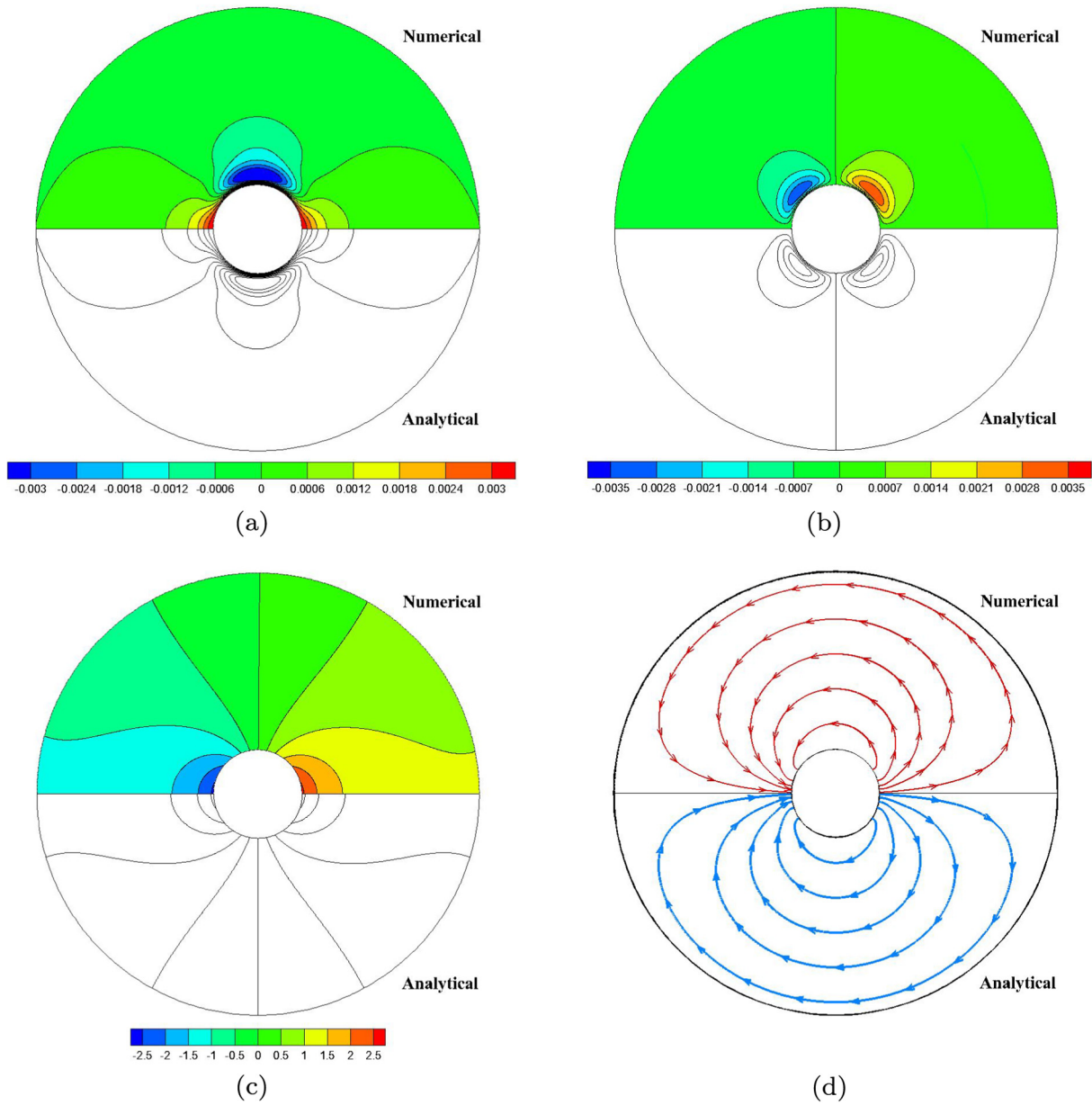


Fig. 6. Analytical and numerical solutions for mineral oil at  $t = 0.2$  s. (a) The horizontal fluid velocity. (b) The vertical fluid velocity. (c) The fluid pressure. (d) The streamlines.

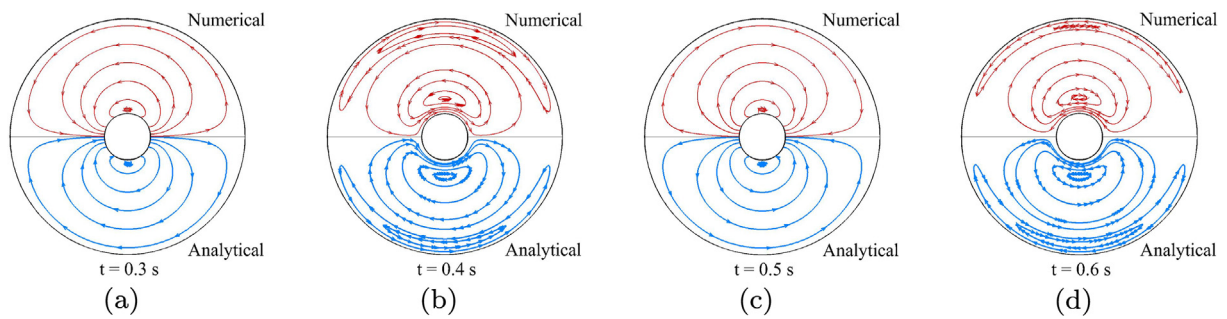


Fig. 7. Analytical and numerical streamline histories for the silicon oil case.

$$\mathbf{J} = -\frac{\kappa_f B_0 (\lambda^2 + \omega^2) \Delta l}{\omega} \left[ E_1 \frac{R_1^2}{r^2} - E_2 \right] \sin \theta e^{-\lambda t + i \omega t} \hat{\mathbf{e}}_r + \frac{\kappa_f B_0 (\lambda^2 + \omega^2) \Delta l}{\omega} \left[ E_1 \frac{R_1^2}{r^2} + E_2 \right] \cos \theta e^{-\lambda t + i \omega t} \hat{\mathbf{e}}_\theta \quad (42)$$

and the fluid Lorentz force is thus

$$\mathbf{J} \times \mathbf{B} = \frac{\kappa_f B_0^2 (\lambda^2 + \omega^2) \Delta l}{\omega} \left[ E_1 \frac{R_1^2}{r^2} + E_2 \right] \cos \theta e^{-\lambda t + i \omega t} \hat{\mathbf{e}}_r + \frac{\kappa_f B_0^2 (\lambda^2 + \omega^2) \Delta l}{\omega} \left[ E_1 \frac{R_1^2}{r^2} - E_2 \right] \sin \theta e^{-\lambda t + i \omega t} \hat{\mathbf{e}}_\theta \quad (43)$$

The electrical current and the Lorentz force here will affect the fluid velocity, pressure, and the viscous force. The cylinder motion will then be influenced and coupled with the fluid and electromagnetic fields in an implicit way.

Upon substituting Eqs. (36) and (43) into (32) and integrating (32), the fluid pressure is obtained as

$$p = p_0 + \frac{\eta (\lambda^2 + \omega^2) \Delta l}{\omega R_1} \left\{ C_3 \left[ -2\alpha \left( \frac{R_1}{r} \right) + \xi r \alpha^2 + 2\xi r \left( \frac{R_1}{r} \right)^2 \right] I_0(\xi r) - C_3 \alpha^2 I_1(\xi r) + C_4 \left[ 2\alpha \left( \frac{R_1}{r} \right) - \xi r \alpha^2 - 2\xi r \left( \frac{R_1}{r} \right)^2 \right] K_0(\xi r) - C_4 \alpha^2 K_1(\xi r) \right\} \cos \theta e^{-\lambda t + i \omega t} + (i\omega - \lambda) \frac{\rho_f R_1 (\lambda^2 + \omega^2) \Delta l}{\omega} \left\{ C_1 \left( \frac{R_1}{r} \right) - C_2 \left( \frac{r}{R_1} \right) - C_3 [\xi r I_0(\xi r) - I_1(\xi r)] + C_4 [\xi r K_0(\xi r) + K_1(\xi r)] \right\} \cos \theta e^{-\lambda t + i \omega t} - \frac{\kappa_f B_0^2 r (\lambda^2 + \omega^2) \Delta l}{\omega} \left[ E_1 \frac{R_1^2}{r^2} - E_2 \right] \cos \theta e^{-\lambda t + i \omega t} \quad (44)$$

where  $p_0$  is the referential pressure. For a Newtonian fluid, the stress tensor  $\sigma_f$  is expressed by

$$\sigma_f = -p\mathbf{I} + \eta (\nabla \mathbf{u}_f + \nabla \mathbf{u}_f^T) \quad (45)$$

with  $\mathbf{I}$  the identity tensor. Substituting Eqs. (36) and (44) into Eq. (45),  $\sigma_f$  is then obtained:

$$\sigma_f = \sigma_{rr} \hat{\mathbf{e}}_r \hat{\mathbf{e}}_r + \sigma_{r\theta} \hat{\mathbf{e}}_r \hat{\mathbf{e}}_\theta + \sigma_{\theta r} \hat{\mathbf{e}}_\theta \hat{\mathbf{e}}_r + \sigma_{\theta\theta} \hat{\mathbf{e}}_\theta \hat{\mathbf{e}}_\theta \quad (46)$$

where

$$\begin{aligned} \sigma_{rr} = & -p - \frac{2\eta (\lambda^2 + \omega^2) \Delta l}{\omega R_1} \left\{ 2C_1 \left( \frac{R_1}{r} \right)^3 + C_3 \left[ -\alpha \left( \frac{R_1}{r} \right) I_0(\xi r) + 2 \left( \frac{R_1}{r} \right)^2 I_1(\xi r) \right] \right. \\ & \left. + C_4 \left[ \alpha \left( \frac{R_1}{r} \right) K_0(\xi r) + 2 \left( \frac{R_1}{r} \right)^2 K_1(\xi r) \right] \right\} \cos \theta e^{-\lambda t + i \omega t} \\ \sigma_{r\theta} = & \sigma_{\theta r} = -\frac{\eta (\lambda^2 + \omega^2) \Delta l}{\omega R_1} \left\{ 4C_1 \left( \frac{R_1}{r} \right)^3 + C_3 \left[ -2\alpha \left( \frac{R_1}{r} \right) I_0(\xi r) + \left( \alpha^2 + \frac{4R_1^2}{r^2} \right) I_1(\xi r) \right] \right. \\ & \left. + C_4 \left[ 2\alpha \left( \frac{R_1}{r} \right) K_0(\xi r) + \left( \alpha^2 + \frac{4R_1^2}{r^2} \right) K_1(\xi r) \right] \right\} \sin \theta e^{-\lambda t + i \omega t} \\ \sigma_{\theta\theta} = & -p - \frac{2\eta (\lambda^2 + \omega^2) \Delta l}{\omega R_1} \left\{ -2C_1 \left( \frac{R_1}{r} \right)^3 + C_3 \left[ \alpha \left( \frac{R_1}{r} \right) I_0(\xi r) - 2 \left( \frac{R_1}{r} \right)^2 I_1(\xi r) \right] \right. \\ & \left. + C_4 \left[ -\alpha \left( \frac{R_1}{r} \right) K_0(\xi r) - 2 \left( \frac{R_1}{r} \right)^2 K_1(\xi r) \right] \right\} \cos \theta e^{-\lambda t + i \omega t} \end{aligned} \quad (47)$$

The total fluid force exerted on the solid is then given by integrating the stress on the cylinder surface:

$$\mathbf{F}_f = \int_{\Gamma_{FSI}} \sigma_f ds \quad (48)$$

where  $\mathbf{s}$  is the area vector of FSI boundary  $\Gamma_{FSI}$ . Applying a coordinate transformation, the total force  $\mathbf{F}_f$  is then obtained as:

$$\mathbf{F}_f = \left[ (\lambda - i\omega)(1 + 2C_1) + \frac{\kappa_f B_0^2}{\rho_f} (E_1 - E_2) \right] \frac{M(\lambda^2 + \omega^2) \Delta l}{\omega} e^{-\lambda t + i \omega t} \hat{\mathbf{e}}_x \quad (49)$$

Extracting the imaginary part of Eq. (49), we then have the total force in the real domain. From time derivatives of Eq. (28), we know the acceleration is in phase with  $[\cos \omega t - (\lambda/\omega) \sin \omega t]$ , and the velocity is in phase with  $\sin \omega t$ .  $\mathbf{F}_f$  can therefore be successfully separated into these two parts as mentioned in Eq. (23), and finally the added mass and damping coefficients are determined as

$$\begin{aligned} C_M = & -1 - 2\text{Re}(C_1) + (2\lambda/\omega)\text{Im}(C_1), \\ C_V = & 2 \left( 1 + \frac{\lambda^2}{\omega^2} \right) \text{Im}(C_1) + \frac{\kappa_f B_0^2}{\rho_f \omega} (E_1 - E_2) \end{aligned} \quad (50)$$

Now that  $C_M$  and  $C_V$  are obtained, substitute Eqs. (50) into (25), and then substitute (25) into (24) and (26), and we will have

$$\begin{aligned} \lambda(\mathbf{u}_f, p, \varphi, \mathbf{J}) = & \mathcal{F}[\lambda(\mathbf{u}_f, p, \varphi, \mathbf{J}), \omega(\mathbf{u}_f, p, \varphi, \mathbf{J})], \\ \omega(\mathbf{u}_f, p, \varphi, \mathbf{J}) = & \mathcal{G}[\lambda(\mathbf{u}_f, p, \varphi, \mathbf{J}), \omega(\mathbf{u}_f, p, \varphi, \mathbf{J})] \end{aligned} \quad (51)$$

where  $\mathcal{F}$  and  $\mathcal{G}$  represent implicit functions of  $\lambda$  and  $\omega$ . Meanwhile,  $\lambda$  and  $\omega$  are functions of all the fields above. Eq. (51) therefore have established a relation between the vibrating mechanism (indicated by  $\lambda$  and  $\omega$ ), and the characteristics of the coupled system, governed by the constants in  $\mathcal{F}$  and  $\mathcal{G}$ , including both material properties ( $m_s, \rho_f, \eta$ , and  $\kappa_f$ ), and external influences ( $k_s$  and  $B_0$ ). The whole system is thus strongly coupled by these varying parameters and implicit functions.

It should be noted that in Eqs. (36), (39), (42)–(44), (47), (49), the imaginary part of the right hand side shall be extracted to get the final solutions to the fluid velocity, the electrical potential, the current density, the Lorentz force, the fluid pressure, stress, and the total force.

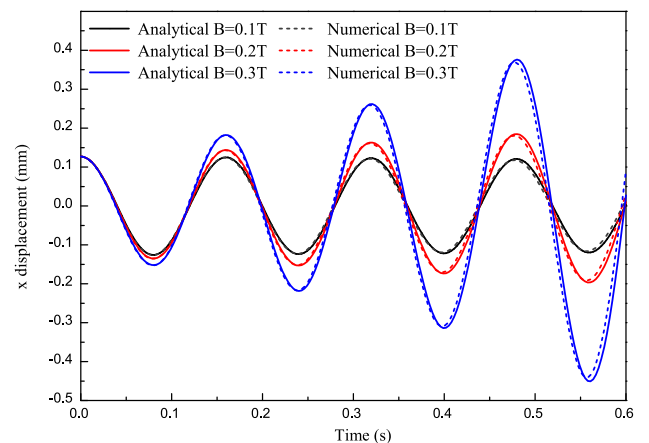
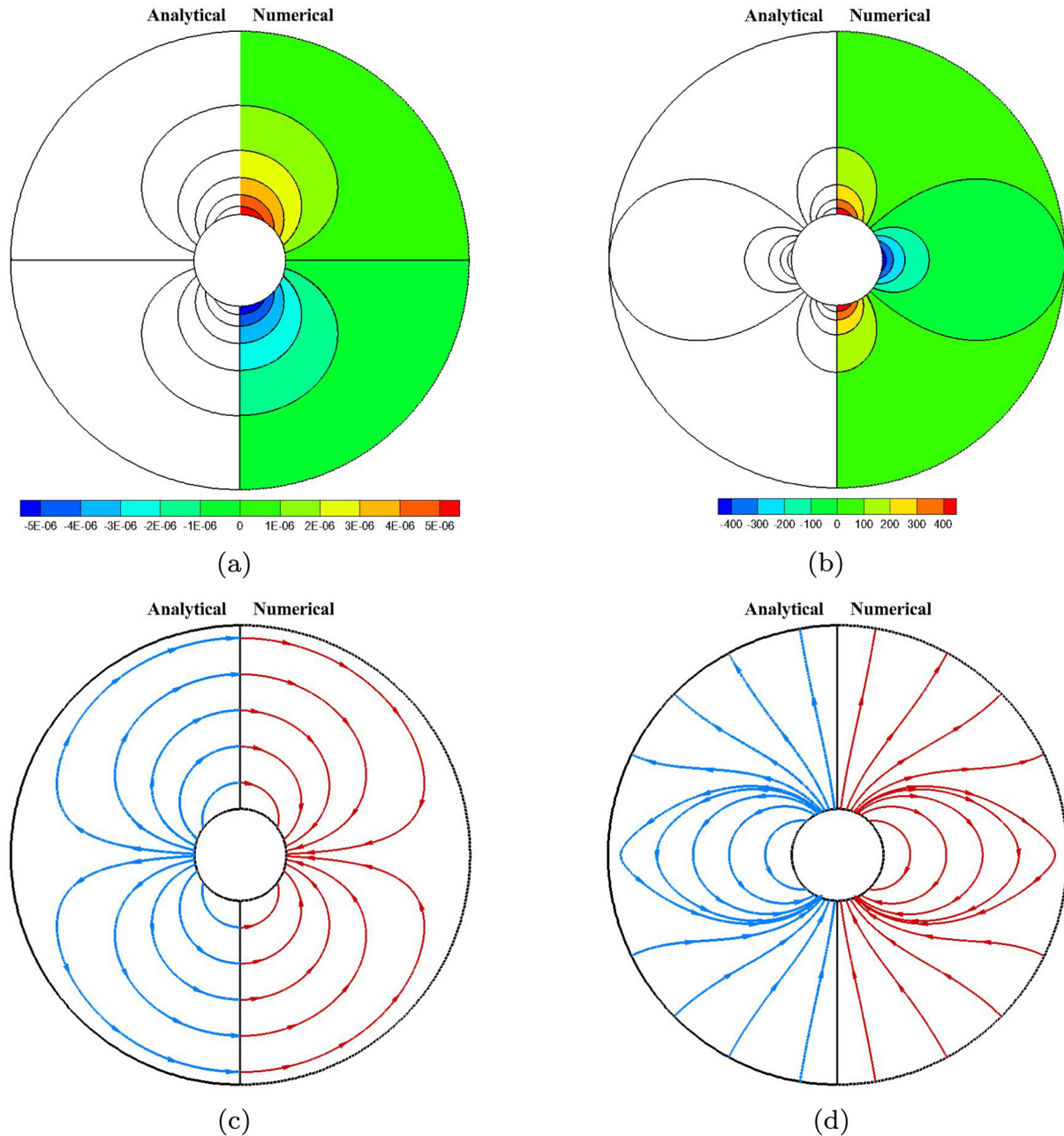


Fig. 8. Analytical and numerical displacement histories for Case I in different magnetic fields (0.1 T, 0.2 T and 0.3 T).



**Fig. 9.** Analytical and numerical solutions for Case I with  $B_0 = 0.1$  T at time  $t = 0.2$  s. (a) The electrical potential distribution. (b) The vertical current density. (c) Streamlines. (d) Electrical current lines.

### 3.3. Application and extension

#### 3.3.1. For general FSI problems

The solutions above, can also be applied on fluid-structure interaction problems without magnetic field influences. For general FSI cases, assuming  $\kappa_f = 0$  or  $B_0 = 0$  in Eqs. (22)–(51), all necessary solutions will be obtained then. To accurately get  $\lambda$  and  $\omega$ , it is suggested to use an iterative way, which could begin with  $\lambda = 0$  and  $\omega = \sqrt{k_s/m_s}$ , and may take less than 10 steps for convergence. Once  $\lambda$  and  $\omega$  are determined, all variables can be obtained.

There are mainly two differences between our solution and Chen et al.'s solution: (1) damping  $\lambda$  is added; (2) frequency  $\omega$  and other relevant quantities are variables, rather than constants. In this way, the strong coupling effect can be taken into account.

The fluid velocity at FSI interface was assumed to be  $\mathbf{u}_f = -\omega \Delta t e^{i\omega t} \mathbf{e}_x$  in Chen et al.'s work, while we used Eq. (29) to introduce damping  $\lambda$  and a non-constant frequency  $\omega$ . Therefore, after the above derivation, we obtained damped fluid velocity and forces, rather than a sinusoidally oscillating fluid field with a constant amplitude in Chen et al.'s work. The damping feature indicates that fluid is influenced by the solid in a time-varying way, rather than a “prescribed” way. The solid is influenced by the fluid in a similar way, and the two-way strong coupling effect is thus taken into account, and leads to more accurate results. Moreover, as we know, the existence of fluid damping in this FSI system is definite, our solution can better described the physical nature of the fluid-solid system by introducing  $\lambda$ .

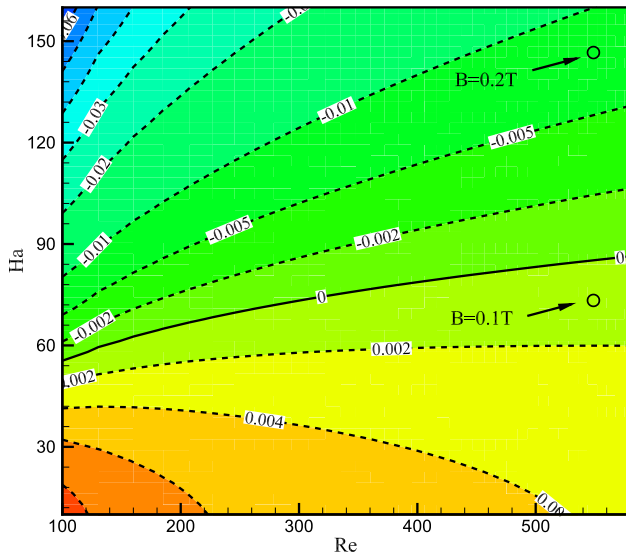


Fig. 10. Diagram of the non-dimensional stability parameter  $\bar{\lambda}$  with respect to the Reynolds number and the Hartmann number.

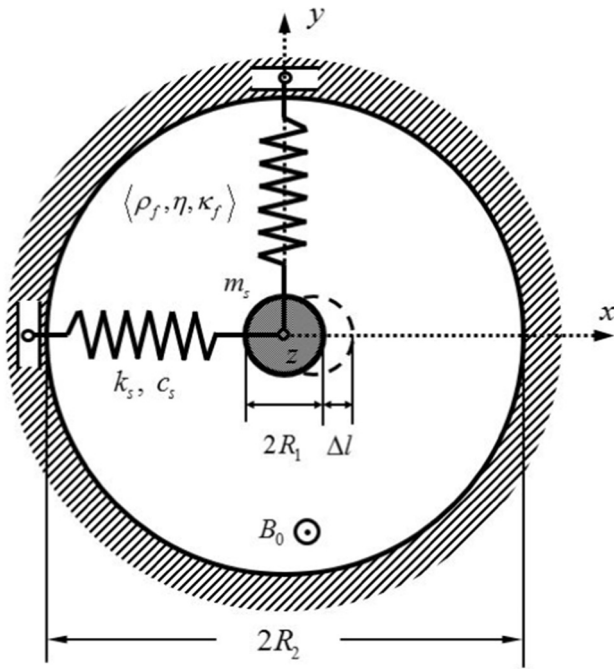


Fig. 11. Geometry of Case II with a vibrating cylinder in fluids with the electrical potential Dirichlet boundary condition.

The differences between our solution and Chen et al.'s solution will be presented in Section 4 by using specific numerical cases.

### 3.3.2. For MFSI problems and further applications

For magneto-fluid-structure interaction problems, the solution above can be used as a benchmark case for verification and validation work. Detailed example cases are presented in Section 5.

The solutions in this paper have potential extensions in the current framework. Since the magnetic field and external power source can excite the vibration, for a very large amplitude, corrections should be made. Another possible extension is for a time-varying external magnetic field. One can substitute  $B_0$  into a time dependent function, and take care of the time integral in Eq. (44). Other possible extensions such as temperature coupling effect

can be expected in the current framework, yet still, the magneto-fluid-structure interaction problem is the main concern in this paper.

## 4. The FSI benchmark case: validation, correction, and extension

### 4.1. Validation of the analytical and numerical approaches

As an example to validate the analytical and numerical methods, we will first present FSI benchmark cases in this section, which have been studied in [26–29]. By reprising this problem, we will present and explain the differences between our method and Chen et al.'s work.

Following the parameters in [27–29], we have  $m_s = 3.408 \times 10^{-1} \text{ kg} \cdot \text{m}^{-1}$ ,  $k_s = 3461.13 \text{ kg} \cdot \text{m}^{-1} \cdot \text{s}^{-2}$ ,  $c_s = 0$ ,  $R_1 = 6.35 \times 10^{-3} \text{ m}$ ,  $R_2 = 5R_1$  and  $\Delta l = 0.02R_1$ . Four types of fluids are calculated, and their properties are: (1) air with  $\rho_{\text{air}} = 1.18 \text{ kg} \cdot \text{m}^{-3}$  and  $\eta_{\text{air}} = 1.82 \times 10^{-5} \text{ Pa} \cdot \text{s}$ ; (2) water with  $\rho_{\text{water}} = 1 \times 10^3 \text{ kg} \cdot \text{m}^{-3}$  and  $\eta_{\text{water}} = 1.33 \times 10^{-3} \text{ Pa} \cdot \text{s}$ ; (3) mineral oil with  $\rho_{\text{m.oil}} = 0.935 \times 10^3 \text{ kg} \cdot \text{m}^{-3}$  and  $\eta_{\text{m.oil}} = 4.1 \times 10^{-2} \text{ Pa} \cdot \text{s}$ ; (4) silicon oil with  $\rho_{\text{s.oil}} = 0.956 \times 10^3 \text{ kg} \cdot \text{m}^{-3}$  and  $\eta_{\text{s.oil}} = 1.45 \times 10^{-1} \text{ Pa} \cdot \text{s}$ . We also define the Reynolds number as  $Re = 2\rho_f\omega R_1\Delta l/\eta$  and the kinematic Reynolds number as  $R_\omega = 4\rho_f\omega R_1^2/\eta$ . The comparison of  $C_M$ ,  $C_V$ , and the solid displacement are first presented. The analytical approach uses Eq. (50) to obtain  $C_M$  and  $C_V$ . The numerical approach evaluates these coefficients by fitting the time-history curve of the solid displacement, using the logarithmic decrement and the damped frequency.

Fig. 2(a) provides our analytical solutions of all four types of fluids, which are used as benchmark results. Fig. 2(b) takes the mineral oil case as an example, and compares our numerical result with the literature. Fig. 3 summarizes the added mass and damping coefficients, by our methods and methods in the literature. It is suggested that both analytical and numerical methods in this paper give very accurate results, even for the most difficult air case [27] considering a very small fluid density.

### 4.2. Accuracy and efficiency of the numerical method

During the calculation of the FSI problems, the displacement prediction-pressure stabilization scheme was applied. Taking the mineral oil case as an example, the accuracy and efficiency of the numerical approach are demonstrated in Fig. 4.

To eliminate the dependence on grids, three sets of unstructured grids (144, 625, and 2500 cells, respectively) were used, and the displacement histories have been given in Fig. 4(a). Despite acceptable accuracy with 625 or 2500 cells, we further used very fine grids (40,000 cells) to get a highly reliable result, which can be used as a future benchmark test. Time step  $\Delta t = 10^{-4} \text{ s}$  was used, and  $\epsilon_{\text{max}} = 10^{-9}$  was chosen as a very strict convergence criterion (which means more sub-steps in each time level). Fig. 4(c) suggests that the average number of sub-steps in each time level will be reduced by the stabilization scheme. It also can be seen in Fig. 4(d), that the calculation using the stabilization scheme can finish after roughly 50,000 sub-steps, while it will take more than 70,000 sub-steps without this method. Fig. 4(d) also suggests that the total fluid force (mainly the pressure) will be greatly smoothed during the iteration. This is due to a smoothed prediction to the fluid boundary displacement, which will affect the solution to the pressure Poisson equation. In this case, the displacement prediction-pressure stabilization scheme ensures the stability by suppressing the pressure oscillation, and enhances

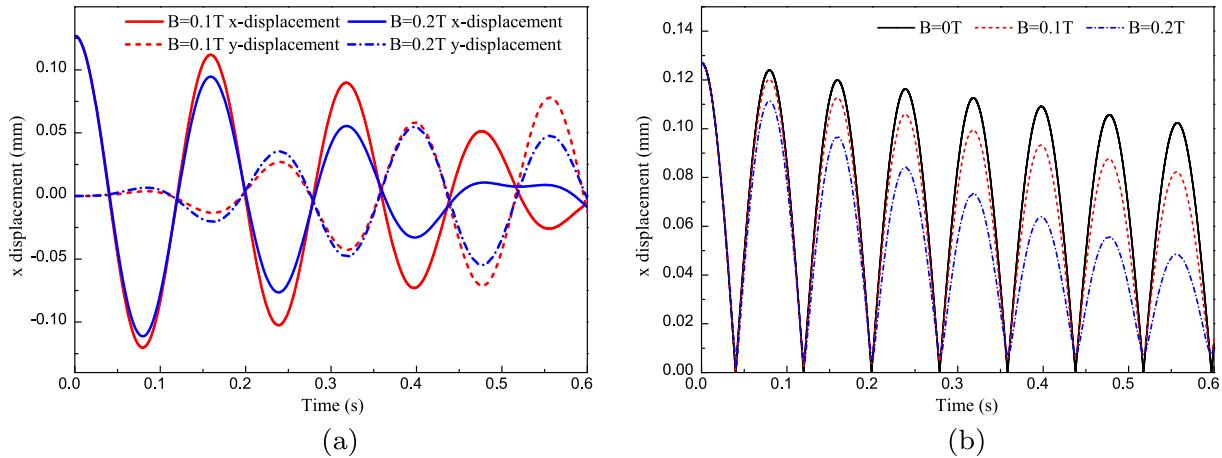


Fig. 12. Displacement histories with different magnetic fields for Case II. (a) Horizontal and vertical displacements. (b) Displacement magnitudes.

the efficiency by reducing 30% of the sub-steps number. Meanwhile, the numerical accuracy will not be reduced by the stabilization scheme, as can be seen in Fig. 4(b).

#### 4.3. Correction and extension to the existing analytical solution

In this section, we will compare our analytical solution, as well as our numerical solution, to the existing analytical solution in [26]. In the work of Chen et al., the suggested parameters for comparison are the added mass coefficient  $C_M$  and the added damping coefficient  $C_V$ . Table 2 lists these coefficients, from the work of Chen et al. and from our analytical and numerical results.

Besides  $C_M$  and  $C_V$ , our analytical solution also gives the solid displacement, the fluid velocity, pressure and stress. These variables were not explicitly given by Chen et al., but can be derived by their  $C_M$  and  $C_V$ . Fig. 5 presents the comparison of the solid displacement, the fluid velocity, pressure and the total force, using the mineral oil case as an example. It is suggested our analytical solution is in accordance with our numerical solution, and differs from Chen et al.'s solution. The solid displacements are similar, while the results of the fluid velocity, pressure and stress are very different. This is mainly because of the different formulations, and the consideration of the amplitude change (indicated by  $\lambda$  and  $\zeta$ ), and the frequency change (indicated by  $\omega$ ) in this paper. Our analytical solution therefore describes the time-varying features with more details, and can improve the accuracy and provide more field variables. Once again, one should keep in mind that, the variables in Fig. 5 were not suggested for final results by Chen et al. The suggested parameters  $C_M$  and  $C_V$  in their work, are very accurate.

Fig. 6 demonstrates detailed results of the mineral oil case at time  $t = 0.2$  s, comparing the analytical and the numerical methods in this paper. These two approaches agree well and can provide benchmark references for future comparisons. Fig. 7 gives the streamline history of the silicon oil case from 0.3 s to 0.6 s, with four representative stages (moving right, reaching the rightmost position, moving left, and reaching the leftmost position). The analytical and numerical streamlines at symmetrical positions are illustrated, and the results are very close. Vortices generated by the vibration are also clearly obtained by both methods. Due to a higher accuracy and a larger solution range, we believe our analytical solution can be applied as a correction ( $C_M$ ,  $C_V$ , and  $\mathbf{d}_s$ ) and extension ( $\mathbf{u}_f$ ,  $p$ ,  $\boldsymbol{\sigma}_f$ , and  $\mathbf{F}_f$ ) to the previous work.

### 5. The magneto-fluid-structure interaction benchmark cases

For the magneto-fluid-structure interaction problems, due to a lack of existing analytical solution, we provide two benchmark

cases using the analytical and the numerical approaches in this paper. The two cases have different electrical potential boundary conditions: (1) Case I with the Neumann boundary condition on the cylinder surface; (2) Case II with the Dirichlet boundary condition on the cylinder surface. The fluid is mercury with  $\rho_{\text{mercury}} = 1.35 \times 10^4 \text{ kg} \cdot \text{m}^{-3}$ ,  $\eta_{\text{mercury}} = 1.56 \times 10^{-3} \text{ Pa} \cdot \text{s}$ , and  $\kappa_{\text{mercury}} = 1.04 \times 10^6 \text{ } \Omega^{-1} \text{m}^{-1}$ .

#### 5.1. Neumann BC for the electrical potential: analytical and numerical approaches

The Neumann boundary condition case follows the analytical solution in Section 3, with  $\partial\varphi/\partial r = 0$  on the cylinder surface, and  $\varphi = 0$  on the container wall. To be noted,  $\partial\varphi/\partial r = 0$  is often used for an insulated stationary wall, but in this case, the wall velocity causes normal electrical current on the cylinder surface. The cylinder can be considered as a time-varying power source, and the input energy may exert the solid vibration. Fig. 8 demonstrates the solid displacement histories with different external magnetic fields ( $B_0 = 0.1 \text{ T}$ ,  $B_0 = 0.2 \text{ T}$ , and  $B_0 = 0.3 \text{ T}$ ). The analytical results are in line with the numerical ones, and both results show increasing amplitudes with relatively strong magnetic fields ( $B_0 = 0.2 \text{ T}$  and  $B_0 = 0.3 \text{ T}$ ), and decaying amplitude with a weak magnetic field ( $B_0 = 0.1 \text{ T}$ ). Fig. 9 provides more detailed distributions of the electromagnetic fields, as well as the streamlines and electrical current lines. The analytical results and the numerical ones meet quite well, in the scope of this paper.

To better understand the mechanism of the electromagnetic influences on the solid motion, let us introduce a non-dimensional parameter  $\bar{\lambda} = \lambda(k_s/m_s)^{-0.5}$ , indicating the stability of the coupled system.  $\bar{\lambda} > 0$  and  $\bar{\lambda} = 0$  respectively suggest decaying and constant vibration amplitudes, meaning the system is stable. While  $\bar{\lambda} < 0$ , the amplitude will increase with time, making the vibration unstable. Choosing various  $k_s$  and  $B_0$ , we will get different Reynolds numbers  $Re = 2\rho_f\omega R_1\Delta l/\eta$  and Hartmann numbers  $Ha = 2R_2B_0\sqrt{\kappa_f/\eta}$ . Using these non-dimensional parameters, the diagram of  $\bar{\lambda}$  has been presented in Fig. 10. It can be seen that, a zero curve has divided the problem into two areas: the stable zone (including the  $B_0 = 0.1 \text{ T}$  case), and the unstable zone (including  $B_0 = 0.2 \text{ T}$  case). This can also be confirmed by the displacement histories in Fig. 8. In fact, since the Lorentz force is in the same direction with the fluid velocity, the electromagnetic effect will always cause increasing amplitudes in this case, unless the viscous force is large enough to balance this effect.

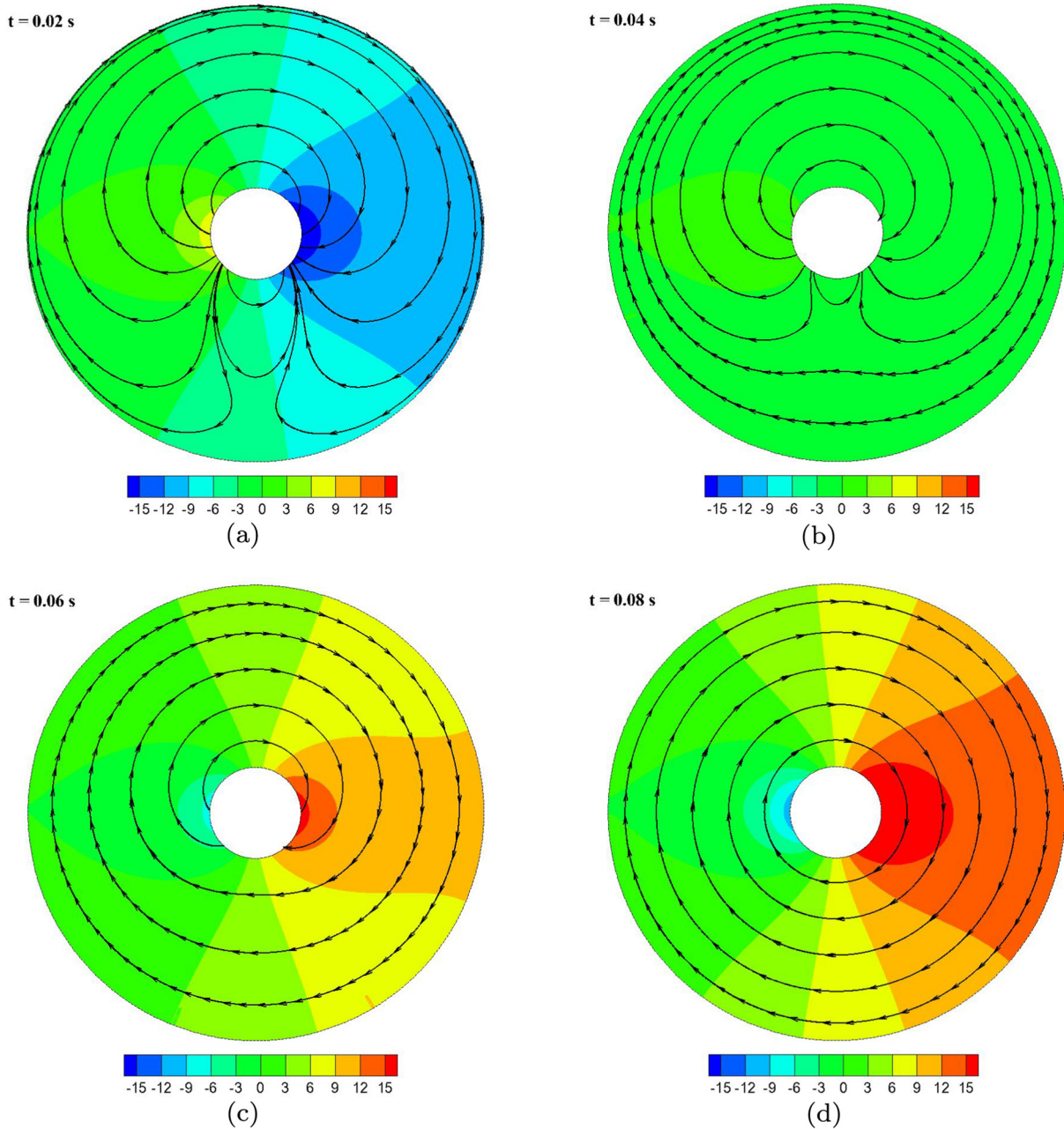


Fig. 13. Numerical solutions for Case II with  $B_0 = 0.1$  T, with background pressure contours and streamlines, at time 0.02 s, 0.04 s, 0.06 s, and 0.08 s, respectively.

5.2. Dirichlet BC for the electrical potential: the numerical approach

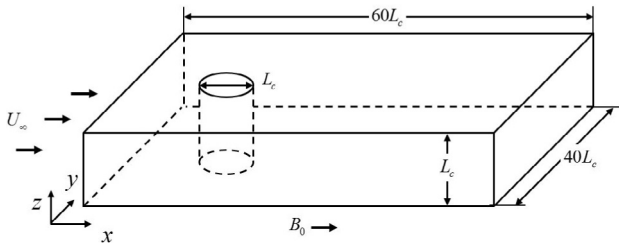
Since the numerical method has been validated by Case I above, the following case is presented only by the numerical method. In this case, the electrical potential boundary conditions are  $\varphi = 1 \times 10^{-4}$  V on the cylinder surface, and  $\varphi = 0$  on the container wall. The cylinder can be treated as a constant voltage power source. In this case, the electrical current is only in the radial direction and the Lorentz force is in the toroidal direction. The solid displacement becomes two-dimensional, and the fluid velocity is no longer symmetric about the  $x$ -axis. An extra spring with the same stiffness  $k_s$  is added to balance the  $y$ -direction fluid force (see Fig. 11).

Fig. 12(a) shows the solid displacements in the  $x$ - and  $y$ -direction, with two different external magnetic fields ( $B_0 = 0.1$  T and  $B_0 = 0.2$  T). The horizontal displacement will decrease with time, and become non-periodical. Fig. 12(b) has presented the

displacement magnitude  $\|\mathbf{d}_s\|_2$ , to demonstrate the damping effect of magnetic fields. It can be seen that a stronger magnetic field will cause larger decrement of the total displacement, which is completely opposite to Case I. In Case II, the toroidal Lorentz force will drive the flow clockwise. Any velocities against this direction will be suppressed, and this process will be accelerated by a stronger magnetic field. Fig. 13 shows the history of streamlines from 0.02 s to 0.08 s, which suggests the change from a vibration induced flow into a MHD dominated flow. This process will repeat for several times afterwards, but eventually, both the solid and the fluid will be rotating without any radial velocities.

6. Transversely oscillating cylinder in a freestream under magnetic fields

In a fusion blanket module, an oscillating structure is a possible way to induce MHD turbulence and enhance heat transfer



**Fig. 14.** Geometry of a transversely oscillating cylinder in freestream under a magnetic field.

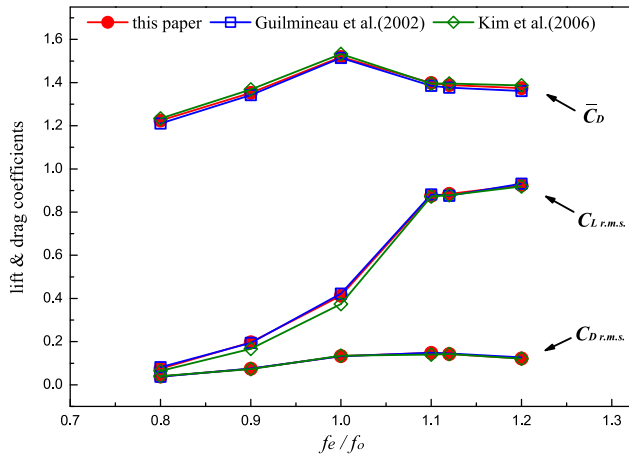


**Fig. 15.** Force coefficients variation with respect to  $f_e/f_0$  with  $N = 0$ .  $\bar{C}_D$ ,  $C_{L,r.m.s.}$  and  $C_{D,r.m.s.}$  denote mean drag coefficient, r.m.s. lift and drag fluctuation coefficients, respectively.

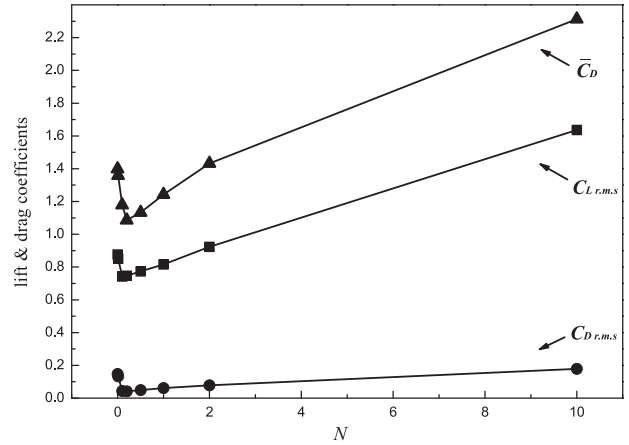


**Fig. 17.** Force coefficients variation with respect to  $N$ , with  $Re = 185$  and  $f_e/f_0 = 1.1$ .  $\bar{C}_D$ ,  $C_{L,r.m.s.}$  and  $C_{D,r.m.s.}$  denote mean drag coefficient, r.m.s. lift and drag fluctuation coefficients, respectively.

efficiency. We now consider a circular cylinder transversely oscillating in a freestream under an external magnetic field. The geometry is given in Fig. 14. Unlike the previous MFSI cases, the solid motion in this case is pre-defined. The problem then becomes a one-way coupled case, yet still very helpful to the study of MHD issues under influences of solid motion.

To minimize the boundary effects, the simulation domain is large enough in the streamwise and transverse directions. The cylinder surface satisfies kinematic boundary condition in Eq. (8) and is electrically insulated. The inlet has a uniform fluid velocity  $U_{\infty}$  and the outlet pressure is zero. Other walls are considered as slip boundaries, and the electrical potential is set to zero on the upper and lower boundaries. A uniform external magnetic field  $B_0$  exists in the streamwise direction. Simulation results suggest

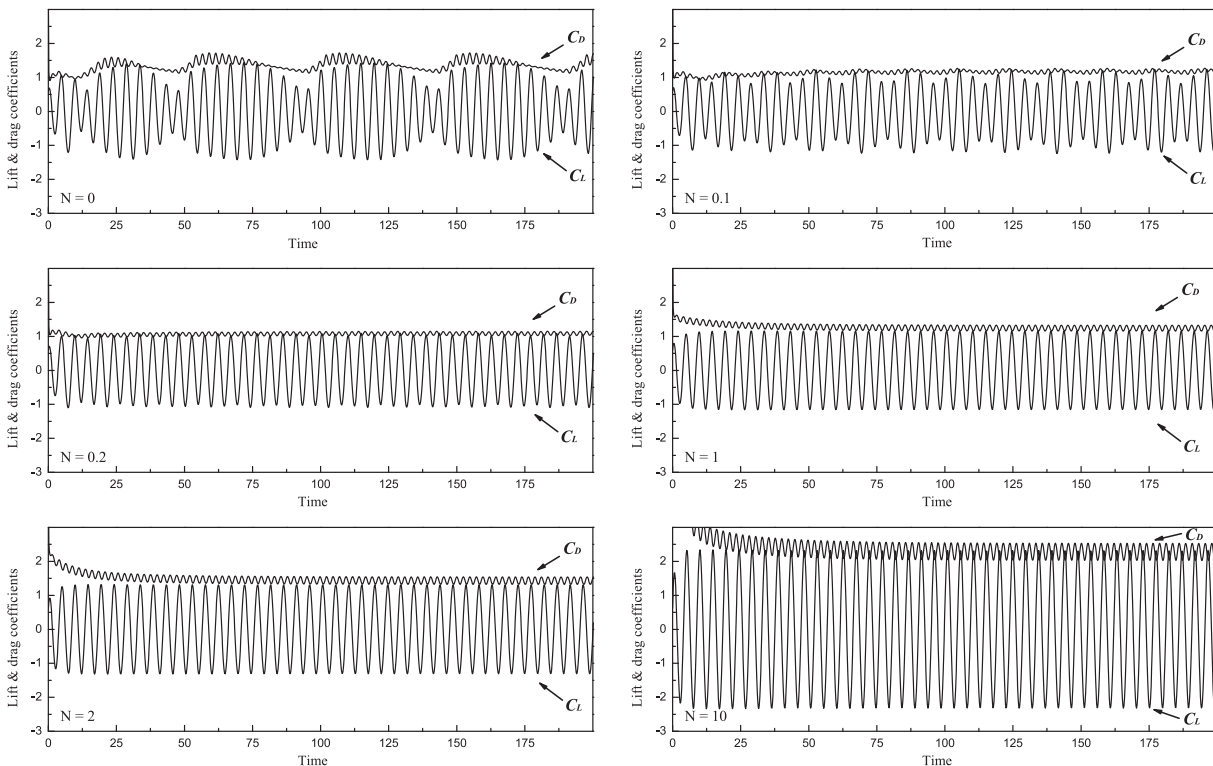


**Fig. 16.** Time histories of lift & drag coefficients for  $Re = 185$  and  $0 \leq N \leq 10$ . The non-dimensional time is  $tU_{\infty}/L_c$ .

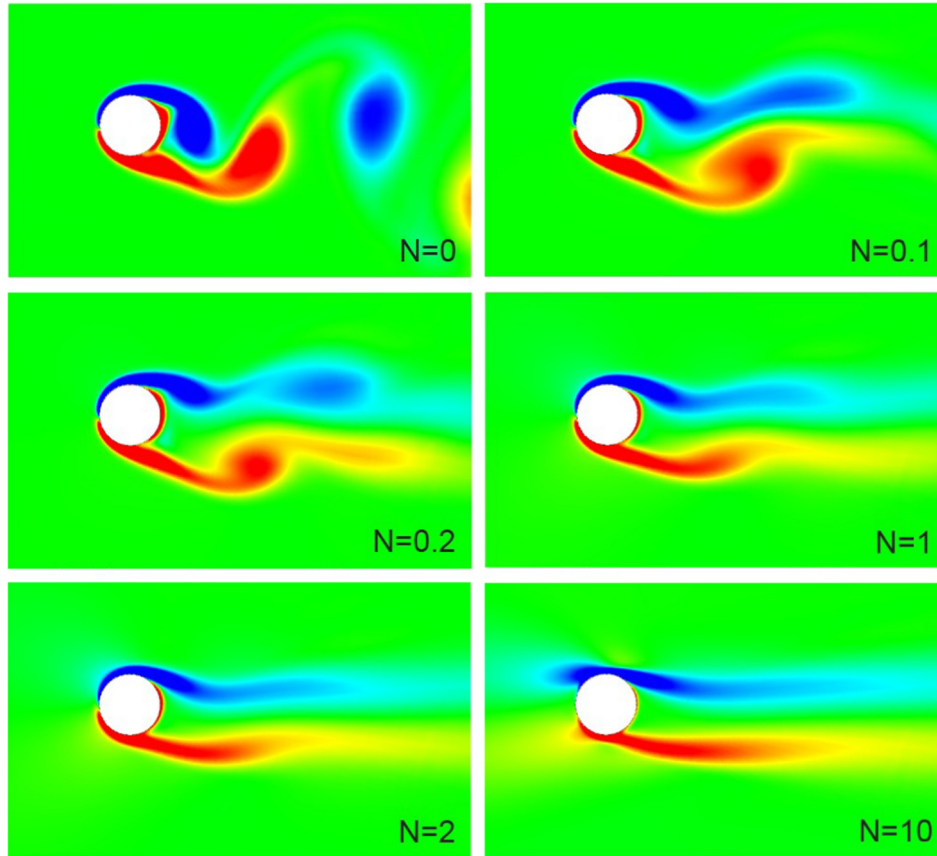


**Fig. 18.** Instantaneous vorticity contours for  $0 \leq N \leq 10$ ,  $Re = 185$  and  $f_e/f_o = 1.1$ . The cylinder is at its extreme upper position.

quasi-2D characteristics, which is suitable to be compared with 2D simulation results without magnetic fields in the literature [33,34].

The Reynolds number in this problem is defined as:

$$Re = \frac{\rho_f L_c U_\infty}{\eta} \quad (52)$$

where  $\rho_f$  and  $\eta$  are fluid density and viscosity, respectively.  $L_c$  is the diameter of the cylinder. The interaction parameter (or Stuart number) is defined as:

$$N = \frac{\kappa_f B_0^2 L_c}{\rho_f U_\infty} \quad (53)$$

where  $\kappa_f$  is the fluid electrical conductivity. The interaction parameter  $N$  describes the ratio of Lorentz forces over inertia forces. The Hartmann number  $Ha$ , expressing the ratio of Lorentz forces over viscous forces, is then

$$Ha = \sqrt{ReN} = L_c B_0 \sqrt{\frac{\kappa_f}{\eta}} \quad (54)$$

The motion of the cylinder is given by a harmonic form:

$$d_c = A_m \cos(2\pi f_e t) \quad (55)$$

where  $d_c$  is the  $y$ -direction location of the cylinder,  $A_m$  is the oscillation amplitude, and  $f_e$  is the oscillation frequency. In the following cases, we have  $Re = 185$ ,  $A_m = 0.2L_c$ , and  $0.8 \leq f_e/f_o \leq 1.2$  as in Guilmineau and Queutey [33], with  $f_o$  the natural shedding frequency of a fixed cylinder. Considering the magnetic effects, we have  $0 \leq N \leq 10$ , or  $0 \leq Ha \leq 43$ .

First, numerical cases with  $N = 0$  were simulated, i.e. cases without magnetic field influences. Fig. 15 shows the mean drag coefficient ( $\bar{C}_D$ ), and the r.m.s. lift & drag fluctuation

coefficients ( $C_{Lr.m.s.}$  &  $C_{Dr.m.s.}$ ). Results for  $f_e/f_o = 0.8, 0.9, 1.0, 1.1, 1.12$ , and  $1.20$  were presented, and the variations of force coefficients with respect to  $f_e/f_o$  are in line with 2D simulations in [33,34].

Let us now consider the influences caused by streamwise magnetic fields. Fig. 16. provides time histories of lift & drag coefficients of the cylinder, taking into account the magnetic field influences. The Reynolds number is  $Re = 185$  and the frequency is fixed as  $f_e/f_o = 1.1$ . Results for  $N = 0, 0.1, 0.2, 1, 2$ , and  $10$  were presented. For the  $N = 0$  case,  $C_D$  and  $C_L$  time histories are in good agreement with [33]. As the magnetic field strength increases, the force coefficients become harmonic. Fig. 17 summarizes  $\bar{C}_D$ ,  $C_{Lr.m.s.}$  and  $C_{Dr.m.s.}$  with respect to  $N$ . As can be seen, the force coefficients will first decrease, then increase with respect to the interaction parameter. At about  $0.1 \leq N \leq 0.3$ , or  $4.3 \leq Ha \leq 7.4$ , an extreme point can be found.

In order to explain the nonlinear effects caused by magnetic field influences, the vorticity contours, streamlines and pressure coefficient are given in Figs. 18–20. For all results, the cylinder is at its extreme upper position. For the pressure coefficient distribution,  $\theta$  is measured clockwise starting from the front stagnation point.

For the  $N = 0$  case, the characteristics of  $C_D$  and  $C_L$  are affected by the combination of two aspects: (1) the natural vortex shedding of a stationary cylinder; (2) the forced vibration of the cylinder. As a result, time histories of  $C_D$  and  $C_L$  in Fig. 16 suggest beat frequency as the difference between  $f_o$  and  $f_e$ . When the magnetic field is taken into account, the streamwise flow will not be directly affected by Lorentz forces. However, the transverse flow will be greatly suppressed by electromagnetic effects. For a stationary cylinder, vortices will be diminished by streamwise magnetic fields, and the flow will be turned into steady [35]. Thus, for

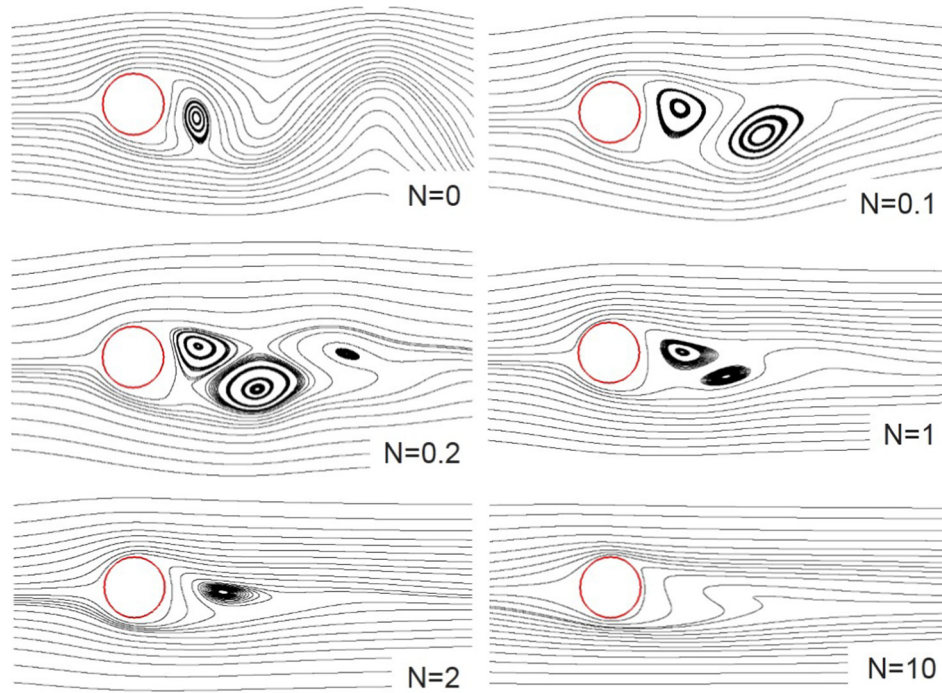


Fig. 19. Instantaneous streamlines for  $0 \leq N \leq 10$ ,  $Re = 185$  and  $f_e/f_o = 1.1$ . The cylinder is at its extreme upper position.

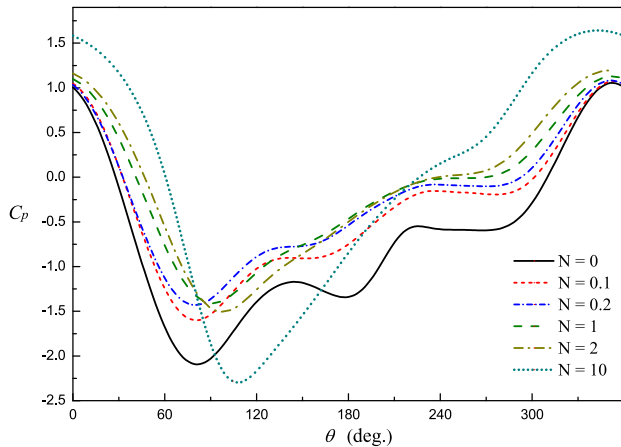


Fig. 20. Pressure coefficients with  $0 \leq N \leq 10$ ,  $Re = 185$  and  $f_e/f_o = 1.1$ . The cylinder is at its extreme upper position, and  $\theta$  measures clockwise starting from the stagnation point.

$N = 0-0.2$ , we can see that the beat feature gradually disappears, and the effects of  $f_o$  on  $C_D$  &  $C_L$  diminishes. In Figs. 18 and 19, vortices are elongated in the streamwise direction, and the fluctuated streamlines are limited to a narrow range. Due to the damping effects of the magnetic field, pressure differences around the cylinder (Fig. 20) decrease with  $N = 0-0.2$ , leading to smaller drag force and lift force fluctuation.

When  $N > 0.2$ , the frequencies of  $C_D$  &  $C_L$  are mainly decided by  $f_e$ , and the natural vortex shedding are fully diminished. As the magnetic field becomes stronger, the forced vortex shedding will also be suppressed (Fig. 18). In this case, the boundary layer surrounding the cylinder will be forced to move transversely as the cylinder oscillates. Since the transverse fluid velocity will be suppressed by the magnetic field, a strong drag force will be generated by Lorentz forces in the boundary layer. This explains the increase of force coefficients when  $N > 1$  (Fig. 17).

To be concluded, the streamwise magnetic field affects the system from two aspects: (1) diminishing vortices shedding, and reducing the force coefficients; (2) suppressing transverse flow caused by the forced vibration, and increasing the force coefficients. These effects are coupled together, and explain the turning point in Fig. 17.

## 7. Concluding remarks

For magneto-fluid-structure interaction problems, an analytical solution and a conservative numerical scheme have been presented. The analytical model in this paper has a simple geometry, but is very challenging due to strong coupling effects of multi-physical fields. For further studies on MFSI problems, this problem is suitable as a beginning case and a benchmark test. The following conclusions have been made.

- (1) For general fluid-structure problems, a strongly coupled correction and extension has been established, comparing with the previous analytical work. By considering the varying features of the vibrating system, the corrected solution improves the accuracy of added mass and damping coefficients, and solid displacement. Besides, the fluid velocity, pressure and stress have been accurately provided, which has extended the previous solution range.
- (2) The analytical solution to the magneto-fluid-structure interaction problem has been derived, and has been validated by the numerical method. The analytical results for further comparison include: the fluid velocity, pressure and stress; the solid displacement; the added mass and damping coefficients of the system; the electrical potential, current density and the Lorentz force.
- (3) The numerical approach for magneto-fluid-structure interaction studies has been developed, and a displacement prediction-pressure stabilization technique has been applied. This stabilization scheme will effectively smooth the pressure oscillation and enhance the iterative efficiency.

- (4) In the magneto-fluid-structure interaction algorithm, a conservative scheme of current density and Lorentz forces for deformed grids has been developed on unstructured grids. Numerical results suggest good accuracy and stability, and a group of benchmark cases for MFSI problems have been successfully established, by the methods above. Considering the vibrating cylinder in quiescent fluid or cross flow, magnetic fields will cause nonlinear effects. The electromagnetic excitation and suppression influences were discussed, and the turning point was presented.

The analytical solution, together with the benchmark cases presented, are suitable for future validation and verification work, with respect to new techniques in magneto-fluid-structure interaction studies. The numerical method developed above, is expected to be applied on further MFSI areas, including the fusion technologies.

### Acknowledgements

The authors acknowledge the support from the NSFC (Natural Science Foundation of China) under Grants No. 51776194 and No. 51376175.

### Appendix A. Supplementary material

Supplementary data associated with this article can be found, in the online version, at <https://doi.org/10.1016/j.compstruc.2018.09.002>.

### References

- [1] Farhat C, Lakshminarayan VK. An ALE formulation of embedded boundary methods for tracking boundary layers in turbulent fluid–structure interaction problems. *J Comput Phys* 2014;263:53–70.
- [2] Cho J, Lee H. Numerical study on liquid sloshing in baffled tank by nonlinear finite element method. *Comput Methods Appl Mech Eng* 2004;193(23):2581–98.
- [3] Mittal R, Seo JH, Vedula V, Choi YJ, Liu H, Huang HH, et al. Computational modeling of cardiac hemodynamics: current status and future outlook. *J Comput Phys* 2016;305:1065–82.
- [4] Tezduyar TE, Schwaab M, Sathe S. Sequentially-coupled arterial fluid-structure interaction (SCAFSI) technique. *Comput Methods Appl Mech Eng* 2009;198(45):3524–33.
- [5] Giacobbi DB, Rinaldi S, Semler C, Paidoussis MP. The dynamics of a cantilevered pipe aspirating fluid studied by experimental, numerical and analytical methods. *J Fluids Struct* 2012;30:73–96.
- [6] Luhar M, Nepf HM. Flow-induced reconfiguration of buoyant and flexible aquatic vegetation. *Limnol Oceanogr* 2011;56(6):2003–17.
- [7] Hu Z, Tang W, Xue H, Zhang X. A SIMPLE-based monolithic implicit method for strong-coupled fluid–structure interaction problems with free surfaces. *Comput Meth Appl Mech Eng* 2016;299:90–115.
- [8] Shelley MJ, Zhang J. Flapping and bending bodies interacting with fluid flows. *Annu Rev Fluid Mech* 2011;43:449–65.
- [9] Shercliff J. The flow of conducting fluids in circular pipes under transverse magnetic fields. *J Fluid Mech* 1956;1(6):644–66.
- [10] Hunt J. Magnetohydrodynamic flow in rectangular ducts. *J Fluid Mech* 1965;21(4):577–90.
- [11] Tian F-B, Dai H, Luo H, Doyle JF, Rousseau B. Fluid–structure interaction involving large deformations: 3D simulations and applications to biological systems. *J Comput Phys* 2014;258:451–69.
- [12] Pathak A, Raessi M. A 3D, fully eulerian, VOF-based solver to study the interaction between two fluids and moving rigid bodies using the fictitious domain method. *J Comput Phys* 2016;311:87–113.
- [13] Long T, Hu D, Wan D, Zhuang C, Yang G. An arbitrary boundary with ghost particles incorporated in coupled FEM-SPH model for FSI problems. *J Comput Phys* 2017;350:166–83.
- [14] Tanaka M, Masunaga T. Stabilization and smoothing of pressure in MPS method by quasi-compressibility. *J Comput Phys* 2010;229(11):4279–90.
- [15] Chen Z-P, Zhang X, Qiu X-M, Liu Y. A frictional contact algorithm for implicit material point method. *Comput Meth Appl Mech Eng* 2017;321:124–44.
- [16] Bukač M, Čanić S, Muha B. A partitioned scheme for fluid–composite structure interaction problems. *J Comput Phys* 2015;281:493–517.
- [17] Zhang Q, Hisada T. Studies of the strong coupling and weak coupling methods in FSI analysis. *Int J Numer Meth Eng* 2004;60(12):2013–29.
- [18] Bathe K-J, Ledezma GA. Benchmark problems for incompressible fluid flows with structural interactions. *Comput Struct* 2007;85(11):628–44.
- [19] Banks JW, Henshaw WD, Schwendeman DW. An analysis of a new stable partitioned algorithm for FSI problems. Part I: incompressible flow and elastic solids. *J Comput Phys* 2014;269:108–37.
- [20] Michler C, Van Brummelen E, Hulshoff S, De Borst R. The relevance of conservation for stability and accuracy of numerical methods for fluid–structure interaction. *Comput Methods Appl Mech Eng* 2003;192(37):4195–215.
- [21] Degroote J, Vierendeels J. Multi-level quasi-Newton coupling algorithms for the partitioned simulation of fluid–structure interaction. *Comput Methods Appl Mech Eng* 2012;225:14–27.
- [22] Causin P, Gerbeau J-F, Nobile F. Added-mass effect in the design of partitioned algorithms for fluid–structure problems. *Comput Methods Appl Mech Eng* 2005;194(42):4506–27.
- [23] Förster C, Wall WA, Ramm E. Artificial added mass instabilities in sequential staggered coupling of nonlinear structures and incompressible viscous flows. *Comput Methods Appl Mech Eng* 2007;196(7):1278–93.
- [24] Balsara DS, Dumbser M. Divergence-free MHD on unstructured meshes using high order finite volume schemes based on multidimensional Riemann solvers. *J Comput Phys* 2015;299:687–715.
- [25] Ni M-J, Munipalli R, Morley NB, Huang P, Abdou MA. A current density conservative scheme for incompressible MHD flows at a low magnetic reynolds number. Part I: on a rectangular collocated grid system. *J Comput Phys* 2007;227(1):174–204.
- [26] Chen S, Wambsgans M, Jendrzejczyk J. Added mass and damping of a vibrating rod in confined viscous fluids. *J Appl Mech* 1976;43(2):325–9.
- [27] Nomura T, Hughes TJ. An arbitrary Lagrangian-Eulerian finite element method for interaction of fluid and a rigid body. *Comput Methods Appl Mech Eng* 1992;95(1):115–38.
- [28] Ishihara D, Yoshimura S. A monolithic approach for interaction of incompressible viscous fluid and an elastic body based on fluid pressure Poisson equation. *Int J Numer Meth Eng* 2005;64(2):167–203.
- [29] Wang S, Khoo BC, Liu G, Xu G, Chen L. Coupling GSM/ALE with ES-FEM-T3 for fluid–deformable structure interactions. *J Comput Phys* 2014;276:315–40.
- [30] Küttler U, Wall WA. Fixed-point fluid–structure interaction solvers with dynamic relaxation. *Comput Mech* 2008;43(1):61–72.
- [31] Ni M-J, Munipalli R, Huang P, Morley NB, Abdou MA. A current density conservative scheme for incompressible MHD flows at a low magnetic reynolds number. Part II: on an arbitrary collocated mesh. *J Comput Phys* 2007;227(1):205–28.
- [32] Issa RI. Solution of the implicitly discretised fluid flow equations by operator-splitting. *J Comput Phys* 1991;93(2):388–410.
- [33] Guilmineau E, Queutey P. A numerical simulation of vortex shedding from an oscillating circular cylinder. *J Fluids Struct* 2002;16(6):773–94.
- [34] Kim D, Choi H. Immersed boundary method for flow around an arbitrarily moving body. *J Comput Phys* 2006;212(2):662–80.
- [35] Mutschke G, Gerbeth G, Shatrov V, Tomboulides A. The scenario of three-dimensional instabilities of the cylinder wake in an external magnetic field: a linear stability analysis. *Phys Fluids* 2001;13(3):723–34.